Mineralium Deposita
https://doi.org/10.1007/s00126-021-01049-0

ARTICLE

Remelting of a Neoproterozoic arc root: origin of the Pulang and Songnuo porphyry Cu deposits, Southwest China

Dian-Zhong Wang[1,2] · Ruizhong Hu[1,2] · Pete Hollings[3] · Xian-Wu Bi[1,2] · Hong Zhong[1,2] · Li-Chuan Pan[1] · Cheng-Biao Leng[4] · Ming-Liang Huang[1] · Jing-Jing Zhu[1,5]

Received: 1 November 2020 / Accepted: 19 February 2021

Abstract

The reduced nature of the subducting slab has been used to explain the relatively poor endowment of economic porphyry copper deposits in Paleo-Tethyan arc systems. The presence of numerous porphyry Cu deposits in the southern Yidun terrane potentially challenges this model, because these deposits are thought to be the product of Paleo-Tethyan subduction. To investigate this, two representative deposits (i.e., Pulang and Songnuo porphyry Cu deposits) from the southern Yidun terrane have been studied. Zircon U-Pb ages of pre- and syn-mineral porphyries in Pulang are 221 ± 2 Ma (MSWD = 0.89) and 215 ± 2 Ma (MSWD = 1.50), respectively. Zircon and garnet U-Pb ages of the Songnuo syn-mineral porphyry are 217 ± 2 Ma (MSWD = 1.15) and 223 ± 5 Ma (MSWD = 0.97), respectively. The Pulang and Songnuo porphyries both have high whole-rock Sr/Y ratios with minor or no negative Eu anomalies, consistent with derivation from hydrous magmas that underwent minor early plagioclase crystallization but abundant amphibole fractionation. The two porphyry intrusions are characterized by high large-ion-lithophile elements (LILE: Th, U, Ba, Rb) abundances, and low concentrations of high-field-strength elements (HFSE: Nb, Ta, Ti, Zr, Hf). They have similar initial Sr isotope ratios from 0.7055 to 0.7073, ε_{Nd} (t) values from − 4.3 to − 1.6 and zircon ε_{Hf} (t) values of − 1.81 ± 1.34 (n = 47) that are distinct from published results for the Permian–Early Triassic Paleo-Tethyan arc granitoids in the Sanjiang region but similar to the Neoproterozoic arc intrusions in the nearby western Yangtze craton. The Pulang and Songnuo porphyries have relatively high zircon Eu_N/Eu_N^* ratios (0.59 ± 0.04, n = 52) and calculated $\Delta \log fO_2$ (FMQ) values (1.61 ± 0.23, n = 52), consistent with relatively oxidized magmas. This feature is similar to the published data for the Neoproterozoic arc intrusions (Eu_N/Eu_N^* = 0.55 ± 0.08; $\Delta \log fO_2$ (FMQ) = 2.14 ± 0.60), but distinct from the published data for the reduced normal Paleo-Tethyan arc magmas (Eu_N/Eu_N^* = 0.29 ± 0.10; $\Delta \log fO_2$ (FMQ) = − 0.68 ± 0.88). Given that the most recent tectonic reconstruction models suggest that the Paleo-Tethys Ocean closed before ~ 220 Ma, we propose that the Pulang and Songnuo porphyries Cu deposits were formed in a postsubduction setting from oxidized melts generated by reactivating the Neoproterozoic arc root, unrelated to Paleo-Tethyan subduction.

Keywords Pulang and Songnuo porphyries Cu deposits · Paleo-Tethys Ocean · Neoproterozoic arc root · Magmatic oxygen fugacity

Editorial handling: B. Lehmann

✉ Ruizhong Hu
huruizhong@vip.gyig.ac.cn

✉ Jing-Jing Zhu
zhujingjing@vip.gyig.ac.cn

[1] State Key Laboratory of Ore Deposit Geochemistry, Institute of Geochemistry, Chinese Academy of Sciences, Guiyang 550081, People's Republic of China

[2] College of Earth and Planetary Sciences, University of Chinese Academy of Sciences, Beijing 100049, China

[3] Department of Geology, Lakehead University, 955 Oliver Road, Thunder Bay P7B 5E1, Canada

[4] School of Earth Sciences, East China University of Technology, Nanchang 330013, People's Republic of China

[5] Harquail School of Earth Sciences, Laurentian University, 935 Ramsey Lake Road, Sudbury P3E 2C6, Canada

Published online: 08 March 2021

Introduction

Hydrous and moderately oxidized ($\Delta \log fO_2$ (FMQ) +1 to +2) magmas are fertile for the generation of porphyry Cu deposits, as they allow the chalcophile elements (Cu and Au) in melts to be transported to upper crustal level and subsequently into exsolved hydrothermal fluids, leading to the formation of sulfide-rich ores (Richards 2003, 2015; Sillitoe 2010; Hou et al. 2015). In contrast, under reduced conditions ($\Delta \log fO_2$ (FMQ) < 0), early sulfide saturation would occur and deplete the magma in Cu and Au, resulting in the magma being less fertile for later hydrothermal porphyry Cu formation (Hamlyn et al. 1985; Richards 2003, 2009, 2011b; Jugo 2009; Botcharnikov et al. 2011; Wang et al. 2014b). It has been suggested that anoxic conditions might have dominated Paleo-Tethyan subduction systems and related arc magmas, thus explaining the rarity of porphyry Cu deposits within the Paleo-Tethyan orogenic belt (Richards and Şengör 2017). However, the Paleo-Tethyan orogenic belt might not be completely barren, and a number of economic porphyry Cu deposits (e.g., Pulang porphyry Cu-Au deposit with 1625 Mt @ 0.34 % Cu and 0.18 g/t Au; Yang and Cooke 2019) have been found in the eastern Tethyan orogenic belt, particularly in the east of the Sanjiang (Three Rivers: Jinshajiang, Langcangjiang and Nujiang; Fig. 1) region, southwest China, which are thought to be associated with normal Paleo-Tethyan lithospheric subduction. To date, the key controls on porphyry Cu formation in the Paleo-Tethyan orogenic belt are unclear especially within the Sanjiang region.

The Sanjiang region on the southeastern margin of Tibetan Plateau has undergone complex tectonic evolution from Tethyan subduction in the Late Paleozoic to continental collision in the Cenozoic, accompanied by multiple mineralization events (Mo et al. 1993; Deng et al. 2010, 2014). The Paleo-Tethyan Permian to Early Triassic arc igneous rocks are widely distributed in this region, whereas the coeval porphyry Cu-Au deposits are restricted to the east of Sanjiang (Fig. 1; Mo et al. 1993; Wang et al. 2008; Deng et al. 2010, 2014; Li et al. 2011; Yang et al. 2011; Richards and Şengör 2017; Yang and Cooke 2019). Specifically, Paleo-Tethyan arc-related granitic rocks with Permian to Early Triassic ages are largely barren and can be found in the Jiangda–Weixi, Yunxian, and Yaxianqiao belts (Fig. 1; Mo et al. 1993; Jian et al. 2009a; Fan et al. 2010; Zi et al. 2013; Yang et al. 2011; Hennig et al. 2009; Liu et al. 2011; Liu et al. 2018). Granitic intrusions associated with porphyry copper deposits are relatively rare in the region, and were emplaced during the Late Triassic mainly in the south of the eastern Yidun terrane (simplified as the southern Yidun terrane below), including near the

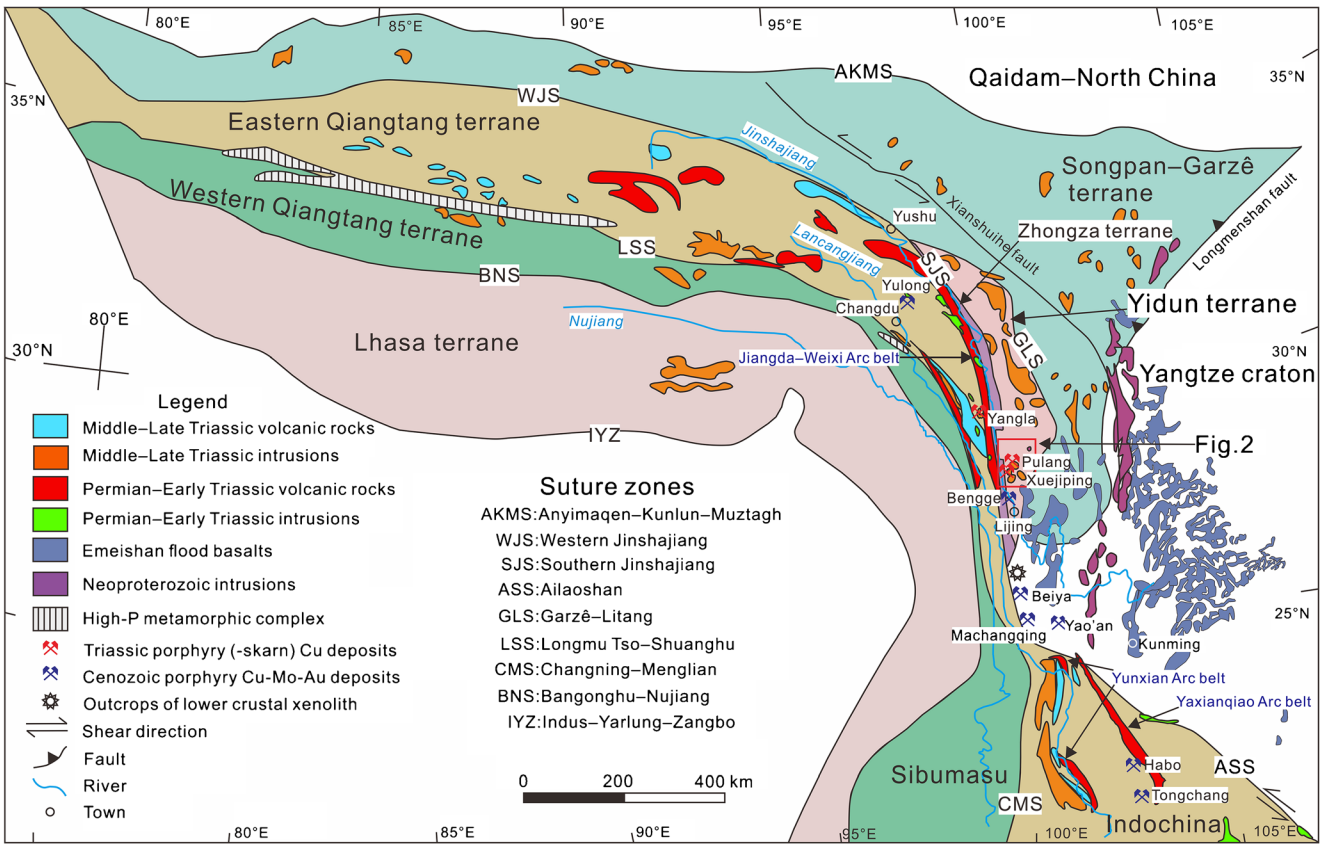

Fig. 1 Tectonic framework of the Sanjiang region, SW China, showing the major terranes, suture zones, arc belts, Permian to Triassic igneous rocks, and locations of the Pulang and other major porphyry Cu deposits, modified from Yang et al. 2014, Xu et al. 2015, Xin et al. 2018, Jian et al. 2009a, and Li et al. 2016

Pulang Cu-Au deposit (Fig. 2; Li et al. 2011; Leng et al. 2012; Chen et al. 2014; Kong et al. 2016; Yang et al. 2017; Cao et al. 2019). In summary, it remains not clear as to why porphyry Cu deposits in the Paleo-Tethyan orogenic belt were only developed in the southern Yidun terrane, Sanjiang region.

In order to explain the spatial and temporal differences in metallogeny within the Sanjiang region, we investigated the magma source and fertility of the Pulang and Songnuo porphyries. By comparing them with the published results for normal Paleo-Tethyan arc igneous rocks, we conclude that the Pulang and Songnuo porphyries formed after the final closure of the Paleo-Tethyan Ocean. It is likely that the relatively high magmatic oxygen fugacity inherited from the partial melting of the Neoproterozoic arc root has played a key role in their formation.

Geological background

The Paleo-Tethys Ocean is the oldest in a series of Phanerozoic ocean basins that closed between Eurasia and Gondwana, starting in the early Late Paleozoic and ending in the Early Mesozoic (Şengör 1979; Şengör et al. 1993; Yin and Harrison 2000; Metcalfe 2002, 2013; Wu and Zheng 2013; Xu et al. 2015; Dai et al. 2017; Wang et al. 2018c; Fang et al. 2020; Xu et al. 2020). The Sanjiang region forms the eastern segment of the Tethyan orogen, on the southeastern margin of the Tibetan Plateau (Fig. 1). From west to east, Sanjiang comprises the Western (South) Qiangtang, Eastern (North) Qiangtang–Indochina, Yidun, and Songpan–Garzê terranes (Fig. 1). They are separated by three major NW-trending Paleo-Tethyan suture zones, which are from west to east the Longmu Tso-Shuanghu–Changning-Mengliang, Jinshajiang–Ailaoshan, and Garzê–Litang zones (Fig. 1). The first suture has been considered to be the major remnant of the Paleo-Tethyan Ocean, whereas the latter two might record small branch or back-arc basins related to Paleo-Tethyan subduction (Yang et al. 2014; Wang et al. 2018c, 2020a). Permian to Early Triassic granitic rocks related to Paleo-Tethyan subduction are widely distributed in Sanjiang, and can be found in the Jiangda–Weixi, Yunxian, and

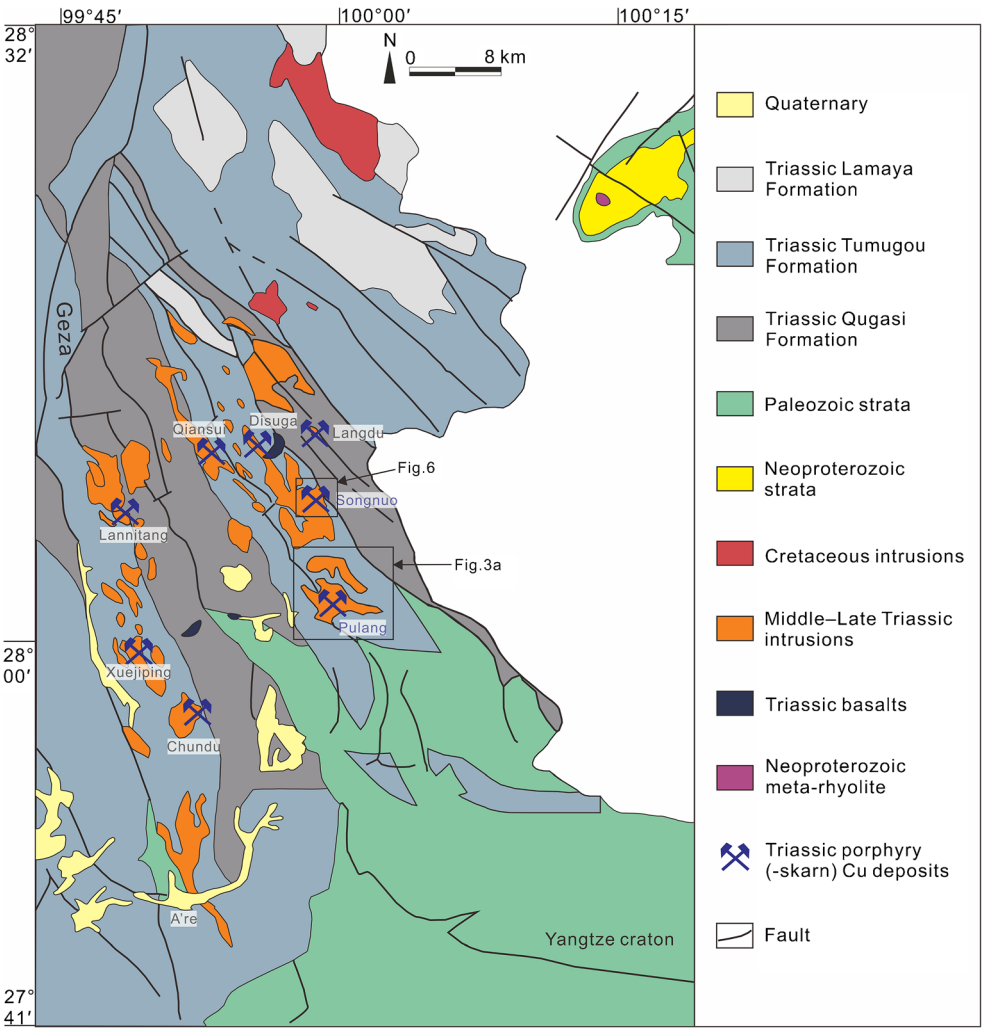

Fig. 2 Geological map of the southern Yidun terrane showing the locations of porphyry Cu deposits, modified from Leng et al. 2014, Kong et al. 2016, Chen et al. 2017, and Tian et al. 2020

Yaxianqiao belts (Fig. 1; Mo et al. 1993; Zhong 1998; Hennig et al. 2009; Jian et al. 2009a; Fan et al. 2010; Liu et al. 2011; Yang et al. 2011; Zi et al. 2013; Liu et al. 2018). The Jiangda–Weixi Arc is defined by a ~ 400-km long series of NW-trending Permian to Early Triassic volcaniclastic and intrusive rocks in the southern part of the Eastern Qiangtang terrane, extending to the west of the Yidun terrane (Fig. 1; Mo et al. 1993; Yang et al. 2011, 2014; Zi et al. 2013; Wang et al. 2014a; Xin et al. 2018). The Yunxian Arc is located in the Indochina terrane and forms a 400-km long by 15–30 km wide sequence of Permian to Early Triassic volcaniclastic successions (Fig. 1; Pan et al. 2012; Dong et al. 2013; Peng et al. 2013; Deng et al. 2018). The ca. 300-km-long Yaxianqiao arc is located on the eastern margin of the Simao terrane and lies parallel to the Ailaoshan ophiolite (Fig. 1). It consists of Permian to Early Triassic calc-alkaline lavas (basalt-andesite-dacite) and sandy to shaley sediments (Zhong 1998; Mo et al. 1998; Jian et al. 2009b; Fan et al. 2010; Liu et al. 2011). There are a number of Late Triassic igneous rocks overlapping with the belt that might have formed in a postcollisional setting (Fig. 1; Peng et al. 2014; Wang et al. 2014a; Li et al. 2019a).

The Yidun terrane can be divided into western and eastern sections based on stratigraphic and structural criteria (Reid et al. 2005). The western Yiduan terrane, also known as the Zhongza terrane (Fig. 1; Chang 1997), comprises a Neoproterozoic basement (Liu et al. 1994; Chang 2000) and an overlying massive basaltic flow with compositions similar to the Emeishan mantle plume flood basalt (Song et al. 2004; Xiao et al. 2005). The Zhongza terrane is widely believed to have rifted from the western Yangtze craton during the Late Permian (Mo et al. 1993; Reid et al. 2005, 2007; Wu et al. 2016; Yang et al. 2014). The western Yangtze craton was the site of extensive oceanic subduction during the early Neoproterozoic, recorded by voluminous arc-like igneous rocks (850–740 Ma; Fig. 1; Zhou et al. 2002; Cawood et al. 2018; Zhao et al. 2018b). The eastern Yidun terrane is dominated by Late Triassic volcano-sedimentary sequences, intruded by voluminous granitic plutons and porphyries with ages from 237 to 206 Ma, with peak magmatism at ~ 216 Ma (Reid et al. 2007; Wang et al. 2011; Leng et al. 2014). The voluminous Late Triassic (~ 216 Ma) igneous rocks within the Yidun terrane have been interpreted to have formed as a result of the westward subduction (in present coordinates) of the Garzê–Litang Ocean (Fig. 1; Hou et al. 1993; Reid et al. 2007; Roger et al. 2010; Wang et al. 2011; Deng et al. 2014; Yang et al. 2017; Leng et al. 2018). In the north of the eastern Yidun terrane, widespread Late Triassic bimodal volcanic suites and arc-type volcanic rocks host multiple sulfide deposits (e.g., the Gacun large Ag-polymetallic VMS deposit; Hou et al. 2003). In the south of the eastern Yidun terrane, numerous Late Triassic intermediate–felsic porphyry bodies contain several porphyry-type or skarn-type Cu-polymetallic deposits or prospects (e.g., Pulang, Xuejiping, Lannitang, Langdu, Songnuo, Qiansui, and Chundu deposits; Fig. 2; Zeng et al. 2003; Leng et al. 2012, 2014; Chen et al. 2014; Kong et al. 2016; Yang et al. 2017; Cao et al. 2019). The presence of Neoproterozoic magmatic rocks (meta-rhyolite) in the southern Yidun terrane implies that it has a Precambrian basement similar to the western Yangtze craton (Fig. 2; Peng et al. 2014; Tian et al. 2020).

Geology of the Pulang and Songnuo porphyry Cu deposits

The southern Yidun terrane contains numerous porphyry–skarn Cu polymetallic deposits associated with Late Triassic magmatism, the largest of which is the Pulang porphyry Cu-Au deposit. The Songnuo deposit is an important exploration target in the southern Yidun terrane, as it has a similar geology, geophysical signature, and geochemical characteristics as the Pulang deposit, but has been the subject of less research (Wu and Dong 2013; Wang and Li 2014; Lai et al. 2016). Therefore, the Pulang and Songnuo porphyry Cu-Au deposits have been studied in this contribution.

Pulang porphyry Cu-Au deposit

The Pulang porphyry Cu-Au deposit (99° 59′ 23″ E and 28° 02′ 19″ N) is located in the southern Yidun terrane, ~ 40 km northeast of Shangri-La, Yunnan province (Li et al. 2011). Pulang is the largest porphyry deposit in the Zhongdian district, and contains proven reserves of ~ 4.31 million t (Mt) of Cu and 113 t of Au with average grades of 0.34 % and 0.09 g/t, respectively (Li et al. 2011). It was discovered in the 1990s and commercial production began in early 2017 with a planned annual production of ~ 50 kt Cu.

The Pulang intrusive complex intruded the Late Triassic andesite and sedimentary rocks of the Tumugou Formation (Fig. 2). The Tumugou Formation is about 5000 m thick and consists of gray slates, sandstones, intermediate-felsic volcanic rocks, and tuffs with minor mafic volcanic rock interlayers. A thick conglomerate layer with poorly sorted pebbles and abundant deformed quartz grains marks the base of the Tumugou Formation (BGMRSP 1991; Wang et al. 2013). There are euhedral pyrite, plant fragments, cross-bedding, ripple marks, and mud pebbles in the Upper Triassic strata indicating a reduced, shallow-water depositional environment (Yang et al. 2014).

The Cu-Au mineralization is mainly hosted in the Pulang intrusive complex (~ 16 km^2), which is composed of five porphyry stock/dike phases (Fig. 3a) including (from oldest to youngest): pre-mineral fine-grained quartz diorite (FQD) and coarse-grained quartz diorite porphyry (CQD; ~ 80 vol%), syn-mineral quartz monzonite porphyry (QMP; ~ 20

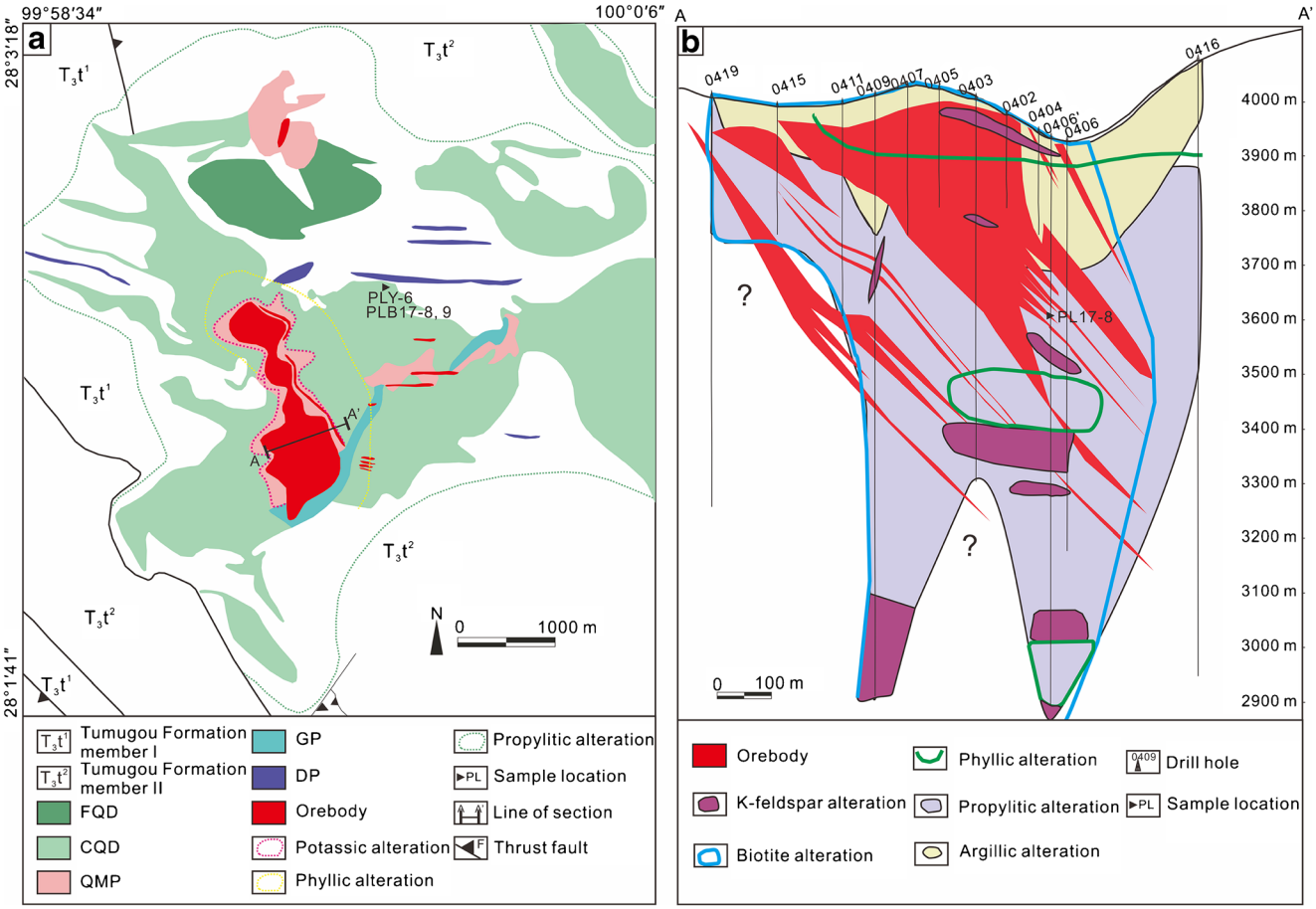

Fig. 3 **a** Geological map of the Pulang porphyry Cu-Au deposit (Modified from Cao et al. 2019) and **b** cross section along section A-A' from Pulang showing alteration zones (Modified after Cao et al. 2019). CQD coarse-grained quartz diorite porphyry, DP diorite porphyry, FQD fine-grained quartz diorite, GP granodiorite porphyry, QMP quartz monzonite porphyry

vol%), and late-mineralization granodiorite porphyry (GP) and diorite porphyry (DP; Leng et al. 2018; Cao et al. 2019). As the CQD and QMP make up the vast majority of the Pulang intrusive complex, they were the focus of this study. The grayish-green CQD is composed of plagioclase (40–50 vol%), amphibole (25–30 vol%), biotite (5 vol%), quartz (5 vol%), and minor K-feldspar phenocrysts in a microcrystalline groundmass (Electronic supplementary materials (ESM) 1 Fig. 1a). The plagioclase phenocrysts are zoned and euhedral to subhedral (1–3 mm). Some plagioclase phenocrysts have fine-grained plagioclase or amphibole inclusions, whereas others are partially overprinted by sericite and have a dissolution structure (ESM 1 Fig. 1c). Euhedral apatite occurs enclosed in amphibole phenocrysts (ESM 1 Fig. 1d). Embayed quartz phenocrysts (400–600 μm) display resorption textures. The gray white QMP is composed of K-feldspar (35–40 vol%), plagioclase (20–25 vol%), quartz (15–20 vol%), biotite (5 vol%), and amphibole (5 vol%; ESM 1 Fig. 1b). The plagioclase phenocrysts (0.5–3.0 mm) and K-feldspar phenocrysts (1–25 mm) are partially overprinted by sericite (ESM 1 Fig. 1e). The euhedral biotite phenocrysts with apatite inclusions are widely distributed in the QMP (ESM 1 Fig. 1f). Accessory titanite and magnetite are euhedral to subhedral (ESM 1 Fig. 1e).

Hydrothermal alteration at Pulang includes potassic, sericite (phyllic), propylitic, and argillic alteration, typical of calc-alkaline porphyry Cu deposits (Seedorff et al. 2005; Sillitoe 2010). The potassic alteration can be subdivided into early K-feldspar alteration and late biotite alteration. The K-feldspar alteration is best preserved in the deep levels of the deposit and spatially associated with the QMP, with minor amounts in the premineral FQD and CQD wall rocks (Figs. 3b and 4). It comprises secondary K-feldspar in the groundmass, K-feldspar replacement of plagioclase and at the edge of plagioclase crystals (ESM 1 Figs. 2a, b). The mineralization is weaker where K-feldspar alteration develops (Fig. 4). Biotite alteration is pervasive in the deposit and mainly associated with the QMP (Fig. 4). It is characterized by secondary biotite with a spherical shape (ESM 1 Fig. 2c), replacing amphibole phenocrysts and in veins (ESM 1 Fig. 2d). Phyllic alteration can be found in both the QMP and CQD (Fig. 4), characterized by a light green color with sericite replacing plagioclase phenocrysts (ESM 1 Figs. 2e, f). The mineralization is weaker where phyllic

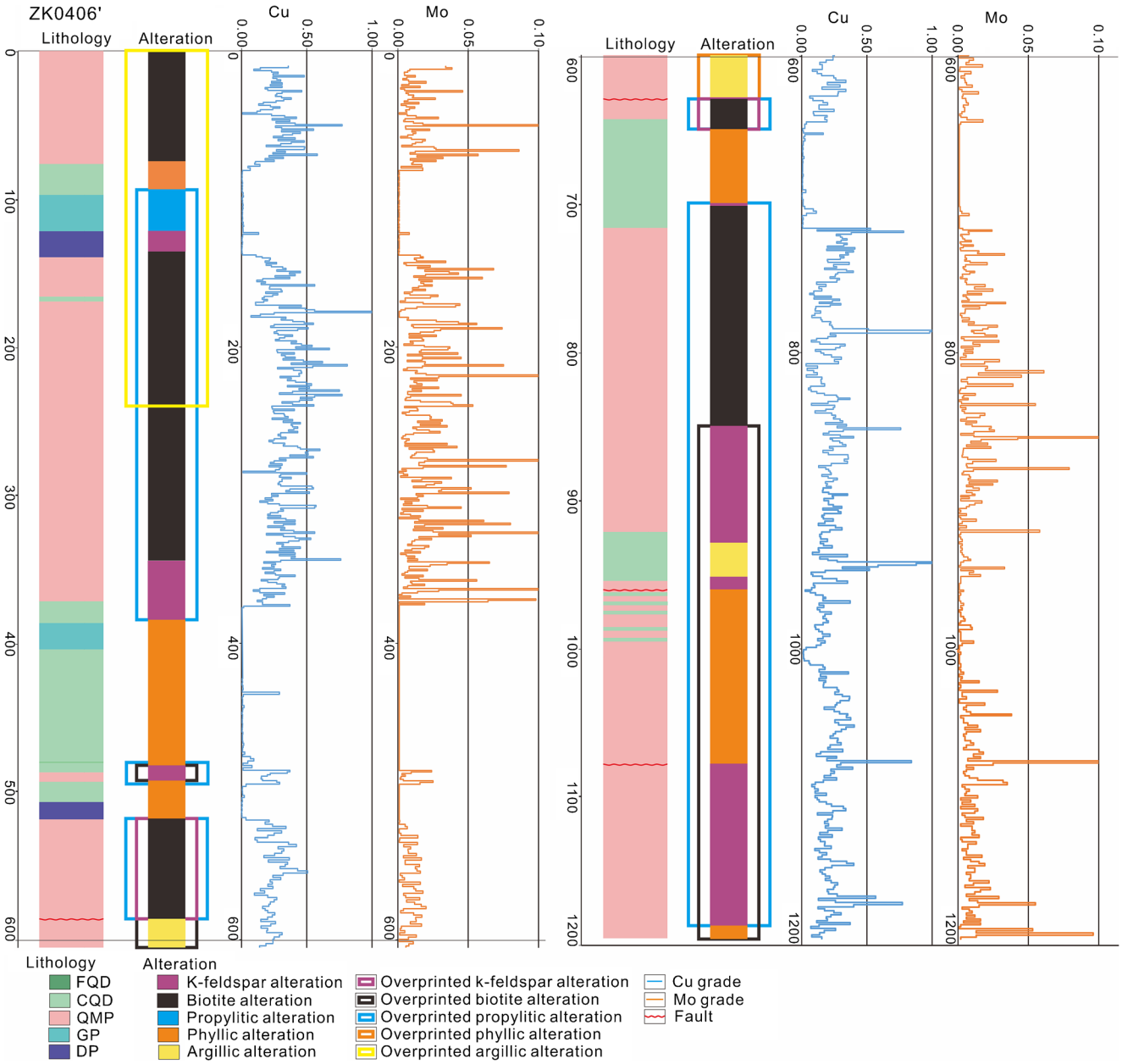

Fig. 4 Drill hole logs showing lithology, alteration, and Cu, Mo grades from diamond hole ZK0406' in the Pulang Cu-Au deposit. Note the close correlations between the QMP unit, biotite alteration, and Cu mineralization. At 100–135 m in drill hole ZK0406', there is propylitic and K-feldspar alteration but no mineralization. The copper and molybdenum grade data are from KPDI (2014). CQD coarse-grained quartz diorite porphyry, DP diorite porphyry, FQD fine-grained quartz diorite, GP granodiorite porphyry, QMP quartz monzonite porphyry

alteration develops (Fig. 4). Propylitic alteration is intensive in the deposit (Fig. 4), and has affected all the intrusive phases (ESM 1 Figs. 1b, 2g). It occurs as chlorite and epidote replacing amphibole and biotite (ESM 1 Fig. 2h). The argillic alteration is mainly distributed on the top of the deposit (Figs. 3b and 4), and can be found in all the intrusive phases comprising illite, kaolinite, and montmorillonite replacement of feldspars (Cao et al. 2019).

In the Pulang porphyry Cu-Au deposit, chalcopyrite is the dominant Cu sulfide mineral (Fig. 5a, b). Native gold mainly occurs as inclusions or veins in chalcopyrite (Fig. 5b). Molybdenite is the dominant Mo sulfide mineral (Fig. 5c), and formed slightly later than chalcopyrite. The Ag mainly occurs as argentite and jalpaite (Fig. 5d). Detailed descriptions of vein styles at Pulang have been given by Cao et al. (2019). There are various vein styles in the Pulang deposit, including USTs, EB, A-, B-, and D-type veins (ESM 1 Fig. 3). USTs, EB, A-, and D-type veins (Gustafson and Hunt 1975) are relatively minor at Pulang, and host only minor amounts of Cu. USTs, EB, and A-type veins (ESM 1 Figs. 3a, b, and c) are mainly found in the middle of the QMP where they are associated with the potassic alteration. B-type quartz veins (Gustafson and Hunt 1975) and

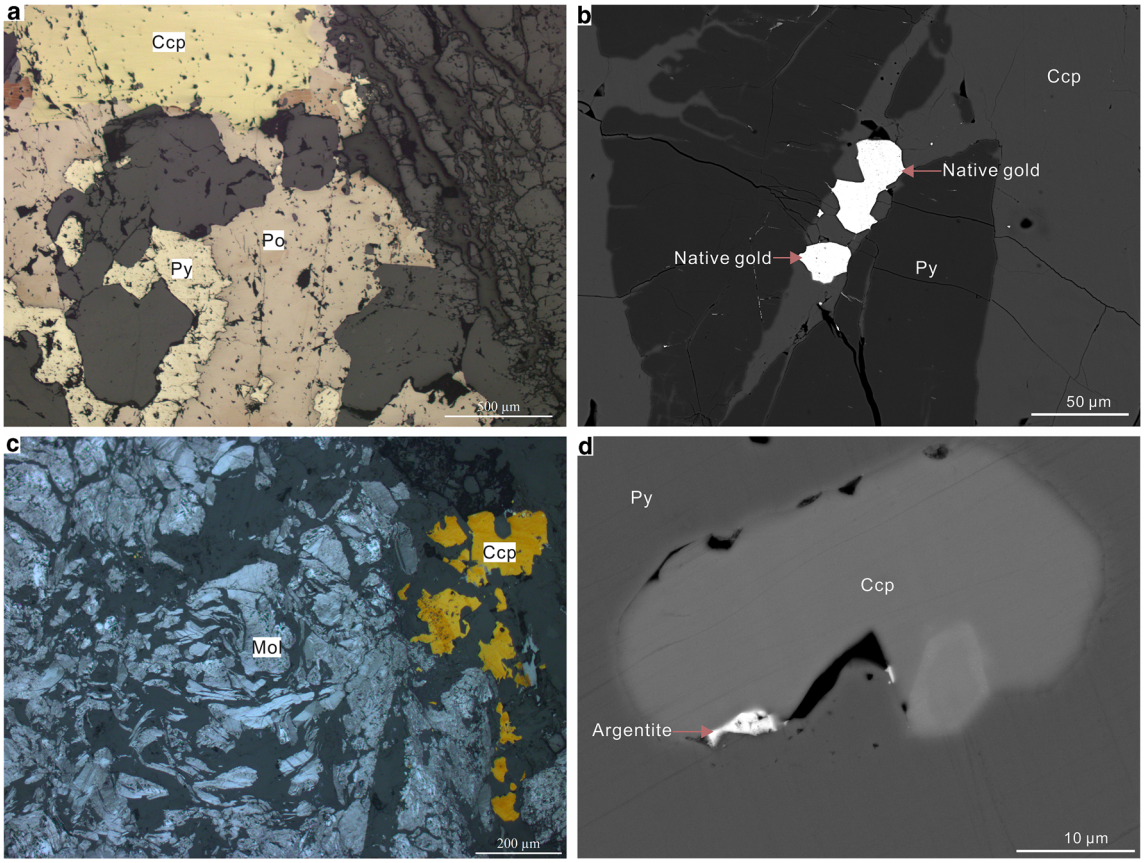

Fig. 5 Photomicrographs of major metal mineral assemblages in the Pulang Cu-Au deposit. **a** Intergrowth of chalcopyrite, pyrite, and pyrrhotite. **b** Pyrite cut by chalcopyrite, and native gold is enclosed by chalcopyrite (BSE image). **c** Chalcopyrite cut by molybdenite (reflected light image). **d** Argentite in a fracture between chalcopyrite and pyrite (BSE image). Ccp chalcopyrite, Mol molybdenite, Po pyrrhotite, Py pyrite

stockworks host the bulk of the copper-gold mineralization. Four types of B-type veins are associated with the biotite and propylitic alteration (ESM 1 Fig. 3). B1 veins have flat boundaries and are mainly associated with biotite alteration (ESM 1 Fig. 3d). B2 veins are characterized by chalcopyrite and pyrite in the middle of the vein, and molybdenite on the edge of the vein (ESM 1 Fig. 3e). B3 veins have more molybdenite and are mainly associated with biotite and propylitic alteration (ESM 1 Fig. 3f). B4 veins contain epidote with the growth direction of epidote and quartz typically perpendicular to the vein boundary (ESM 1 Fig. 3g). D veins are associated with phyllic alteration and contain mainly pyrite with minor quartz and/or tourmaline (ESM 1 Fig. 3h).

Songnuo porphyry Cu deposit

The Songnuo porphyry Cu deposit is located ~ 10 km north of the Pulang porphyry Cu-Au deposit in the southern Yidun terrane (Fig. 2). The current proven ore reserves are ~ 10 Mt with average Cu grade of ~ 0.3% and as such it is a small-scale Cu deposit, but exploration is ongoing (Yu 2018). The Songnuo intrusive complex intruded the Late Triassic andesite and sedimentary rocks of the Qugasi and Tumugou Formations. The Qugasi Formation is located in the northeast of the district (Fig. 6), and is composed of dark gray slates, fine-grained quartz sandstones, limestones, and mafic volcanic rocks with a basal conglomerate unit (BGMRSP 1991). The Tumugou Formation is located in the north and south of the mining area (Fig. 6), where it consists of anhydrite and marble. The Songnuo composite intrusion is mainly composed of three porphyry stock/dike phases (Fig. 6), a quartz diorite (QDP), quartz monzonite porphyry (QMP), and granodiorite porphyry (GP; ESM 1 Fig. 4). The QDP accounts for the majority of the composite intrusion (Fig. 6). Crosscutting relationships between the porphyry intrusions have not been observed.

Hydrothermal alteration of the intrusions at Songnuo includes potassic, sericite (phyllic), propylitic, and skarn alteration. The potassic alteration is characterized by abundant secondary K-feldspar and is spatially associated with the QMP (ESM 1 Fig. 4a). Phyllic alteration is best preserved in the shallow level of the deposit and spatially associated with the QDP and QMP (ESM 1 Figs. 4b, c). It consists of sericite replacing plagioclase phenocrysts and pyrite in the groundmass. Propylitic alteration is intensive in the deposit, and has affected the QDP and QMP. It

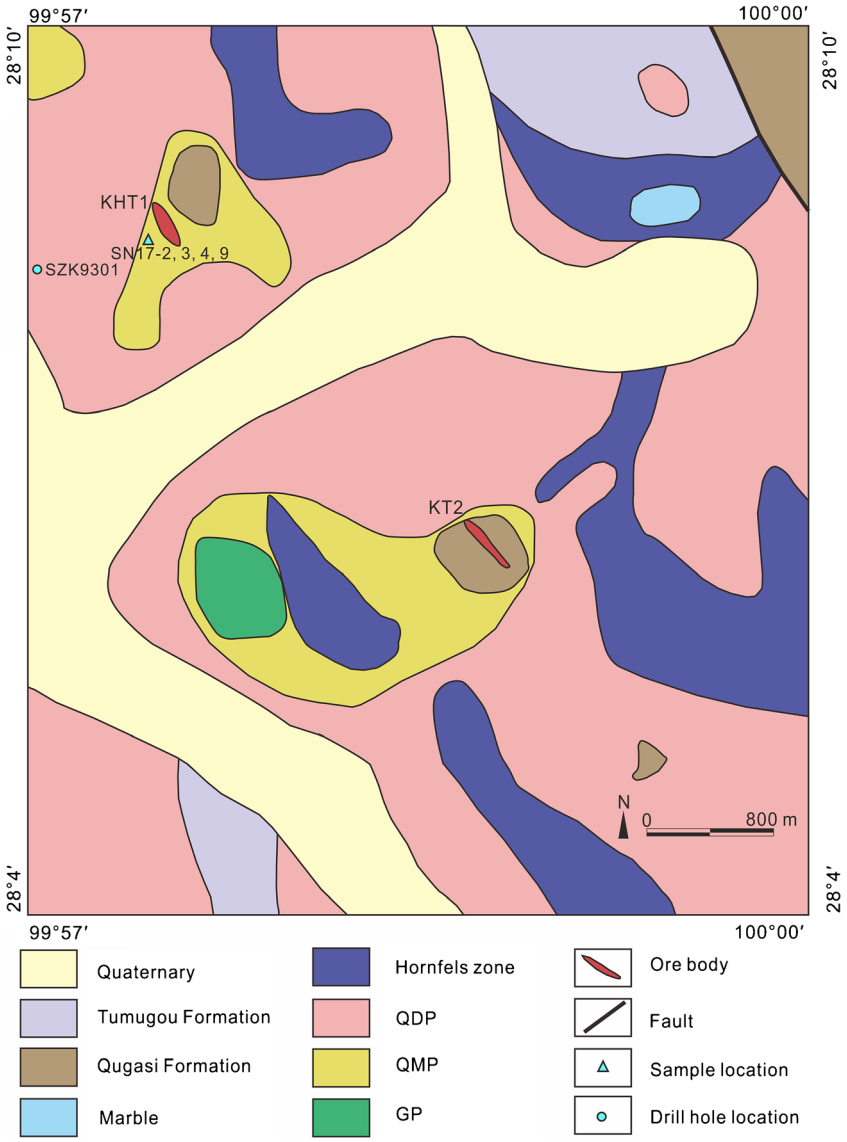

Fig. 6 Geologic map of the Songnuo Cu deposit (Modified from Lai et al. 2016)

comprises chlorite and epidote replacement of amphibole and biotite (ESM 1 Fig. 4d). Skarn alteration is mainly developed at the contact between the QMP and the country rock (ESM 1 Fig. 4e). The skarn minerals are mainly composed of garnet and diopside (ESM 1 Fig. 4f). The main ore minerals are chalcopyrite, galena, sphalerite, pyrite, and magnetite, hosted in the QMP and skarn. The mineralization is mainly in quartz-sulfide veins containing chalcopyrite, pyrite, and quartz (Yu 2018). The late quartz sulfide veins are mainly located at the edge of the porphyries with chalcopyrite, galena, and quartz, and sometimes small amounts of sphalerite (Yu 2018).

Sampling and analytical methods

Nine samples from the Pulang and Songnuo porphyry intrusions were collected from outcrop and drill holes. Detailed descriptions and locations are listed in ESM 2 Table A1. Three least-altered samples from the pre-mineral CQD and one sample from the syn-mineral QMP from the Pulang Cu-Au deposit were chosen for whole-rock analyses. Two of them were prepared for zircon U-Pb dating, Hf isotope, and trace-element measurements. Four relatively fresh samples from the Songnuo QMP were chosen for whole-rock analyses. One of them was prepared for zircon U-Pb dating, Hf isotope, and trace-element measurements. One sample of garnet skarn was chosen for garnet U-Pb dating.

Zircon U-Pb dating and trace-element analyses

Three samples from the Pulang (PLY-6 and PL17-8) and Songnuo (SN17-4) intrusions were chosen for zircon separation, U-Pb dating, and trace-element analyses. Zircon crystals were separated from 3- to 4-kg rock samples at the Langfang

Sincerity Geological Service Co. Ltd., Langfang, China. Selected grains were euhedral, clear, colorless, lacked fluid, and mineral inclusions, and were 200–300 μm in diameter. Grains were mounted in an epoxy resin disc at the Chongqing YuJin Technology Co. Ltd., Chongqing, China. Transmitted and reflected light photos, and cathodoluminescence (CL) images were taken of the zircon grain mounts prior to analysis at the Chongqing YuJin Technology Co. Ltd., Chongqing, China.

For zircon grains from the Pulang and Songnuo intrusions, in situ uranium and lead isotopes and trace-element analyses were conducted synchronously by laser ablation inductively coupled plasma mass spectrometry (LA-ICP-MS: GeoLas Pro 193 nm ArF excimer laser and Agilent 7500x ICP-MS) at the State Key Laboratory of Ore Deposit Geochemistry, Institute of Geochemistry, Chinese Academy of Sciences, Guiyang, China (SKLODG). The laser spot size was around 32 μm, with a 5-Hz pulse rate, and a fluence of ~ 10 J/cm^2. Helium was used as a carrier gas which was mixed with argon via a T-connector before entering the ICP-MS. Each analysis incorporated 60 s of data acquisition from the sample and a background acquisition of approximately 30 s (gas blank). Zircon reference 91500 was used as an external standard to correct U-Pb laser induced elemental fractionation and instrument bias, which was analyzed twice for every 6–8 analyses (i.e., 2 zircon 91500 + 6–8 samples + 2 zircon 91500). Zircon standards Qinghu and Plešovice were used as the unknown samples for age data quality assessment. The measured weighted mean $^{206}Pb/^{238}U$ ages of the reference materials are as follows: 91500 (1062 ± 7 Ma, mean square of weighted deviation (MSWD) = 0.80), Qinghu (163 ± 7 Ma, MSWD = 5.00), and Plešovice (337 ± 6 Ma, MSWD = 3.2; ESM 2 Table A2). They are in good agreement with the reported values (Wiedenbeck et al. 1995; Slama et al. 2008; Li et al. 2013b). All data are reported to 2σ analytical uncertainties. For zircon trace-element compositions, samples were calibrated against multiple-reference materials (NIST 610, BHVO-2G, BCR-2G, BIR-1G) combined with Zr internal standardization. Analytical results for standard NIST 610 (n = 8) and reference values are shown in ESM 2 Table A3. They are consistent with the reference values for most elements (Pearce et al. 1997). Small mineral inclusions (e.g., apatite and rutile) are unavoidable during LA-ICP-MS analyses (e.g., Zhu et al. 2018) and analyses with Ca > 300 ppm or La > 0.3 ppm and Ti > 20 ppm were excluded due to apatite and rutile contamination, respectively. Data processing including off-line selection and integration of background and peak signals, and time-drift correction and quantitative calibration for trace-element analyses and U-Pb dating were performed with ICPMSDataCal 10.2 software (Liu et al. 2010a), and uncertainties on individual analyses were reported at 1σ. The detailed protocols are provided in Liu et al. (2010a, b).

In situ zircon Hf isotope analyses

Hafnium isotopic ratios of zircon were measured by LA-MC-ICP-MS at the SKLODG. An Australian Scientific Instruments RESOlution-LR laser-ablation system and Nu Instruments Nu Plasma III MC-ICP-MS (Wrexham, Wales, UK) were combined for the experiments. The 193 nm ArF excimer laser, homogenized by a set of beam delivery systems, was focused on the zircon surface with a fluence of 6.0 J/cm^2. The ablation protocol used a spot diameter of 40 um at 6 Hz repetition rate for 40 s (equating to 240 pulses). Helium was used as a carrier gas to efficiently transport aerosol to the MC-ICP-MS. Five standard zircons (GJ-1, 91500, Plešovice, Mud Tank, and Penglai) were analyzed every thirty unknown samples and one standard zircon (Penglai) every five samples to ensure quality control. The measured $^{176}Hf/^{177}Hf$ values from the standard Penglai (n = 8) ranged from 0.282877 ± 0.000015 (1σ) to 0.282952 ± 0.000015 (1σ), which agree well with the nominal values within the defined uncertainty (Li et al. 2010). Analytical results are given in Table 3.

Mass bias effects on Hf were corrected using an exponential law and a true value for $^{179}Hf/^{177}Hf$ of 0.7325 (Patchett and Tatsumoto 1981). Correction for isobaric interference of ^{176}Lu on and ^{176}Yb on ^{176}Hf was by using $^{176}Yb/^{173}Yb$ = 0.7962 and $^{176}Lu/^{175}Lu$ = 0.02655 (Vervoort et al. 2004) with an exponential-law mass bias correction assuming $^{173}Yb/^{171}Yb$ ratio of 1.129197 (Vervoort et al. 2004). For the calculation of ε_{Hf} values and Hf isotope model ages, we assumed that the $^{176}Lu/^{177}Hf$ ratio of average crust is 0.015, and the $^{176}Lu/^{177}Hf$ and $^{176}Hf/^{177}Hf$ ratios of present depleted mantle and chondrite are 0.0384 and 0.28325, 0.0332, and 0.282772, respectively (Blichert Toft and Albarède 1997; Griffin et al. 2002). The decay constant of ^{176}Lu used in this study was 1.865 × 10^{-11} (Scherer et al. 2001).

Whole-rock element and isotope analyses

Eight least altered samples were selected for crushing and analyzed by ALS Laboratory Group, Guangzhou, China, for major element analyses. Lithium metaborate fusion followed by X-ray fluorescence spectrometry was used for determination of 12 major elements and loss-on-ignition (LOI). The samples were then analyzed after lithium metaborate fusion by ICP-MS (ELAN DRC-e) for 48 minor and trace-elements at the SKLODG. The detailed analytical procedures are described by Liang et al. (2000). Based on analyses of standards and duplicates, the accuracy for major elements oxides and trace (minor) elements is within five and ten relative percent, respectively.

Eight samples were chosen for measurement of Sr-Nd isotopes at the Nanjing FocuMS Technology Co. Ltd., Nanjing, China. Rock powders were dissolved in 0.5 ml 60 wt% HNO_3 and 1.0 ml 40 wt% HF in sealed high-pressure PTFE bombs at 195 °C for 3 days. Detailed procedures for Rb, Sr, Sm, and Nd purifications were similar to Zhu et al. (2017). The Rb-Sr and Sm-Nd isotope compositions were determined by MC-ICP-MS (Nu Plasma II). Raw data were normalized to $^{86}Sr/^{88}Sr = 0.1194$ for Sr, $^{146}Nd/^{144}Nd = 0.7219$ to correct mass fractionation. Isotope standards (NIST SRM 987 for Sr and JNdi-1 for Nd) were periodically determined to correct instrumental drift. The Nd model ages and ε_{Nd} values were calculated with the assumption that $^{147}Sm/^{144}Nd$ and $^{143}Nd/^{144}Nd$ ratios of the present-day depleted mantle and chondrite are 0.512638, 0.1976, and 0.51315, 0.2137, respectively (Wasserburg et al. 1981; White and Hofmann 1982). Geochemical reference materials USGS BCR-2, BHVO-2, AVG-2, and RGM-2 were used as quality control. The results of the standard analyses are within analytical uncertainty of published results (Weis et al. 2006).

Garnet U-Pb dating

One sample (SN9301-30) from Songnuo was prepared as a standard polished thin section and subsequently examined using optical microscopy and back-scattered electron (BSE) imaging to characterize the mineralogical and textural relationships. BSE was completed using a JSM-7800F field emission scanning electron microscope (FE–SEM) equipped with a TEAM Apollo XL energy dispersive spectroscope at the SKLODG.

For garnet grains, in situ uranium and lead isotope measurements were conducted synchronously by LA-ICP-MS (GeoLas Pro 193 nm ArF excimer laser and Agilent 7500x ICP-MS) at the SKLODG. The laser spot size was around 60 μm, with a 5-Hz pulse rate, and a fluence of ~ 6 J/cm^2, with argon used as the make-up gas which was mixed with helium as the carrier gas via a T-connector before entering the ICP-MS. Each analysis incorporated 60 s of data acquisition from the sample and a background acquisition of approximately 30 s (gas blank). The specific analytical conditions were similar to Deng et al. (2017). The Willsboro Garnet was used as the standard for mass discrimination and U-Pb isotope fractionation (Seman et al. 2017). The garnet standard Mali was used as an unknown for age data quality assessment and yielded a weighted mean $^{206}Pb/^{238}U$ age of 203 ± 2 Ma (MSWD = 0.67) in this study, which is consistent with the recommended value of 202 ± 2 Ma (Seman et al. 2017). Analytical results are given in ESM 2 Table A4. Data processing including off-line selection and integration of background and peak signals, and time-drift correction and quantitative calibration for U-Pb dating were performed using ICPMSDataCal 10.2 software (Liu et al. 2010a).

Results

Zircon U-Pb ages

Zircon U-Pb data for the Pulang and Songnuo porphyries are presented in ESM 2 Table A2. All results are illustrated in Fig. 7 with 2σ errors. All zircons show oscillatory zoning under CL imaging (Fig. 7a, c, and d). Sample PLY-6 was obtained from the Pulang CQD. Analyzed zircon grains from the sample show tightly clustered ages, mostly with low common lead contents (Fig. 7a). Twenty-five spots were analyzed on 25 zircon crystals and all of them form a coherent group with $^{206}Pb/^{238}U$ ages varying from 209 ± 4 to 230 ± 3 Ma (ESM 2 Table A2). They yielded a weighted mean $^{206}Pb/^{238}U$ age of 221 ± 2 Ma (MSWD = 0.85), which is consistent with the concordia age (221 ± 1 Ma; MSWD = 1.3; Fig. 7a, b). Sample PL17-8 was obtained from the Pulang QMP. Zircon grains from PL17-8 exhibit broad oscillatory growth zoning with locally homogeneous patches in the CL images (Fig. 7c). Twenty-five spots were analyzed on 25 zircon grains and all of them form a coherent group with $^{206}Pb/^{238}U$ ages varying from 204 ± 2 to 231 ± 4 Ma (ESM 2 Table A2). They yielded a weighted mean $^{206}Pb/^{238}U$ age of 215 ± 2 Ma (MSWD = 1.5), which is within error of the concordia age (215 ± 1 Ma; MSWD = 5.4; Fig. 7c, d). Sample SN17-4 was obtained from the Songnuo QMP. Twenty-five spots were analyzed on 25 grains and all of them form a coherent group with $^{206}Pb/^{238}U$ ages varying from 209 ± 3 to 226 ± 3 Ma (ESM 2 Table A2). They yielded a weighted mean $^{206}Pb/^{238}U$ age of 217 ± 2 Ma (MSWD = 1.15), which is within error of the concordia age (216 ± 1 Ma; MSWD = 3.3; Fig. 7e, f).

Garnet U-Pb age

Garnet U-Pb age data for sample SN9301-30 from the Songnuo deposit are presented in ESM 2 Table A4. The results are illustrated in Fig. 8 with 2σ errors. The BSE image of the euhedral garnet is uniform (Fig. 8a). The garnet in sample SN9301-30 has high U content (234–679 ppm) and yielded an intercept age of 223 ± 5 Ma (MSWD = 0.97; Fig. 8b) based on 30 analyzed spots.

Whole-rock major and trace-elements

Major and trace-element data for eight whole-rock samples from the Pulang and Songnuo porphyries are listed in Table 1 and illustrated in Figs. 9 and 10. The samples from the Pulang porphyry are relatively fresh as indicated by their low LOI contents of 0.73–1.45 wt% (Table 1). They are felsic and metaluminous in composition (SiO_2 = 61.26–66.17 wt%; molar $Al_2O_3/(CaO + Na_2O + K_2O)$ = 0.73–1.06). On the $Zr/TiO_2 \times 0.0001$ versus Nb/Y diagram, these samples mostly plot in the trachyandesite/syenite fields (Fig. 9a). The rocks

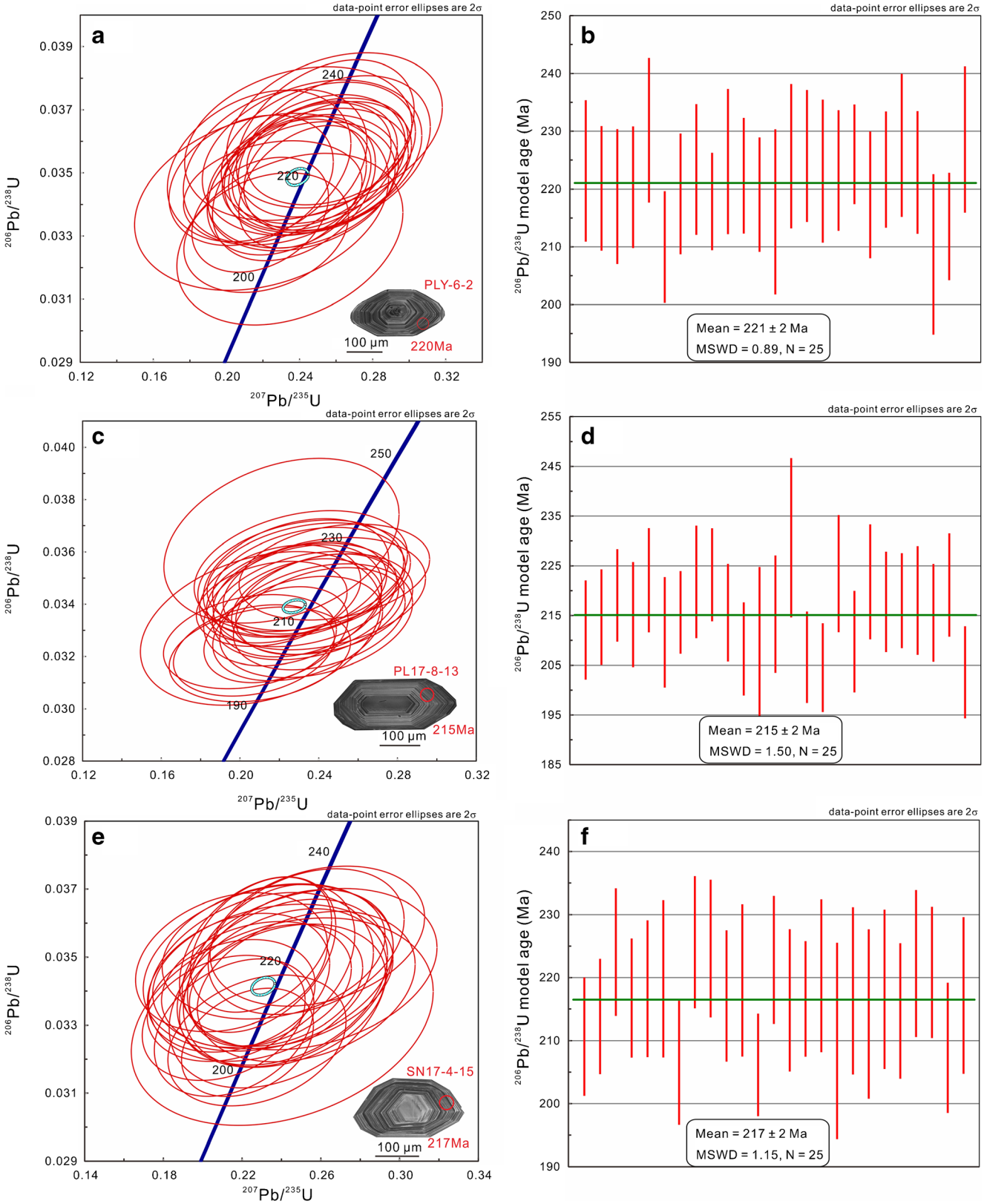

Fig. 7 Zircon LA-ICP-MS U-Pb concordia diagrams for the (**a**) Pulang QDP and (**c**) QMP, and (**e**) Songnuo QMP samples. The weighted mean ages and MSWD are shown for each sample (**b**, **d**, and **f**). Typical CL images of zircons are also shown for each sample

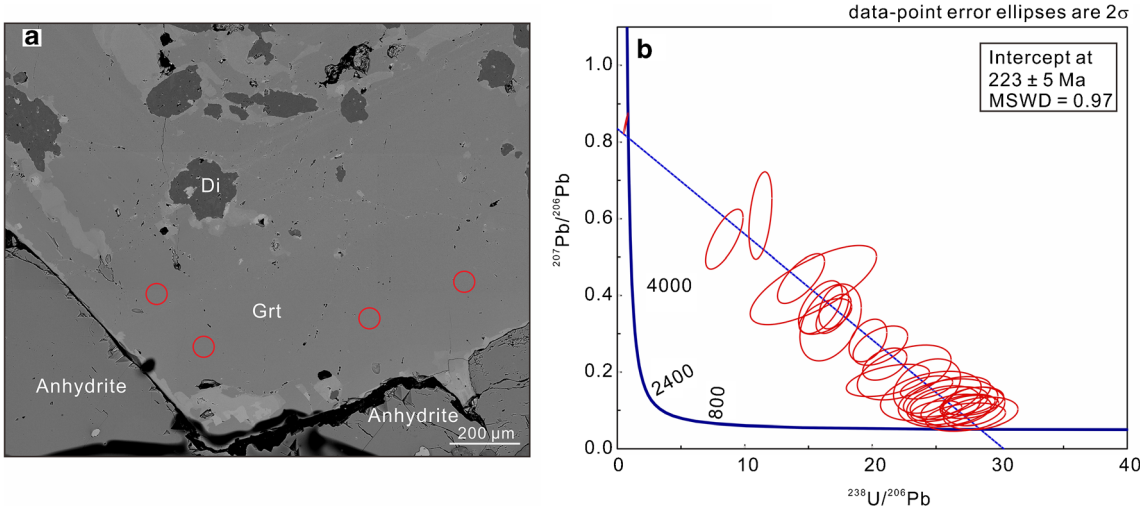

Fig. 8 **a** Homogeneous BSE image of euhedral garnet and **b** U-Pb Tera-Wasserburg concordia diagram for garnet in Songnuo. Di diopside, Grt garnet

have high alkali contents ($Na_2O + K_2O$ = 5.52–7.66 wt%). The content of K_2O varies greatly (0.35–4.29 wt%), probably due to hydrothermal (sodic-potassic) alteration that is present in the ore-related rocks. Most samples have flat or slightly negative Eu anomalies with Eu_N/Eu_N^* values of 0.85–0.99 (n = 4; Fig. 9b), most likely reflecting amphibole fractionation and a lack of plagioclase separation. They have high Sr/Y (46–64; Fig. 9c) and La_N/Yb_N (19–28; Fig. 9d) ratios, similar to adakitic rocks.

The samples from the Songnuo porphyry have variable LOI (3.27–6.53 wt%) consistent with a greater degree of hydrothermal alteration. In general, the HFSE, rare-earth elements (REE), Th, and transition elements are essentially immobile during hydrothermal alteration (Hawkesworth et al. 1997; Wang et al. 2006). In the $Zr/TiO_2 \times 0.0001$ versus Nb/Y diagram, these samples plot at the junction of the rhyodacite/dacite/granodiorite, trachyandesite/syenite, and alkalic-basalt/alkalic-gabbro fields (Fig. 9a). They have small negative Eu anomalies (Eu_N/Eu_N^* = 0.66–0.74; Fig. 9b) and moderate Sr/Y (12–40; Fig. 9c) and La_N/Yb_N (13–19; Fig. 9d) ratios.

The Pulang and Songnuo porphyry samples have similar trace-element compositions. On primitive mantle-normalized trace-element and chondrite-normalized REE diagrams, the porphyry rocks show largely indistinguishable patterns consistent with typical subduction-related igneous rocks (Fig. 10; Hawkesworth et al. 1993; Pearce 1996). Both are characterized by high LILE (Th, U, Rb, Ba) and light rare-earth element (LREE) enrichments, low concentrations of HFSE (Nb, Ta, Zr, Hf, Ti), relative depletions in compatible elements and middle to heavy rare-earth elements (MREE, HREE; La/Yb = 18–40), and flat- to listric-shaped patterns from MREE to HREE. The Songnuo samples have more negative Sr anomalies than those of Pulang, which may be the result of plagioclase fractionation, consistent with the lower Eu_N/Eu_N^* values of the Songnuo samples (Richards and Kerrich 2007).

Whole-rock Sr-Nd isotopes

Sr-Nd isotope data for the Pulang and Songnuo porphyry samples are presented in Table 2 and illustrated in Fig. 11 a. Three samples from the Pulang CQD have initial Sr isotopic ratios from 0.7056 to 0.7058, coupled with $\varepsilon_{Nd}(t)$ values from − 2.2 to − 1.6 (avg. = − 2.0 ± 0.4, n = 3). One sample from the Pulang QMP has initial Sr isotope ratios of 0.7055 with $\varepsilon_{Nd}(t)$ values of − 3.9. Four samples from the Songnuo QMP have initial Sr isotope ratios from 0.7061 to 0.7073, coupled with $\varepsilon_{Nd}(t)$ values from − 4.3 to − 3.6 (avg. = − 3.8 ± 0.34, n = 4). These results do not correlate with LOI values, suggesting minimal effects of hydrothermal alteration (ESM 1 Fig. 5).

Zircon Hf isotopes

Zircon Hf isotope compositions for the Pulang CQD, QMP, and Songnuo QMP are presented in Table 3 and Fig. 11 b. The Pulang CQD has $\varepsilon_{Hf}(t)$ values of − 0.71 ± 1.32 (n = 12), with two-stage Hf model ages of 1297 ± 84 Ma. The Pulang QMP has $\varepsilon_{Hf}(t)$ values of − 1.19 ± 0.84 (n = 10), with two-stage Hf model ages of 1323 ± 53 Ma. The Songnuo QMP has more negative $\varepsilon_{Hf}(t)$ values of − 2.58 ± 1.00 (n = 25), with two-stage Hf model ages of 1413 ± 63 Ma (n = 25).

Zircon trace-element compositions

Fifty-two trace-element spot analyses were obtained on zircons from samples of the Pulang and Songnuo porphyries (ESM 2 Table A3; ESM 1 Fig. 6). All zircon grains are characterized by high HREE and low LREE concentrations, with slightly negative Eu and strongly positive Ce anomalies (ESM 1 Fig. 6). The REE patterns (REE = 322–796 ppm) with Th/U ratios above 0.1 (0.62–1.24) are indicative of igneous zircons (Hoskin and Schaltegger

Table 1 Major and trace element compositions of the Pulang porphyry and Songnuo porphyry

	Pulang porphyry				Songnuo porphyry			
Sample #	PLY-6	PLB17-8	PLB17-9	PLY-8	SN17-2	SN17-3	SN17-4	SN17-9
Weight %								
SiO_2	61.3	61.5	64.0	66.2	65.4	63.3	62.0	55.8
Al_2O_3	14.7	14.9	15.3	15.7	15.0	14.4	14.1	13.8
CaO	4.74	4.69	6.53	2.46	0.730	0.880	1.08	0.420
Fe_2O_3(T)	5.30	5.11	2.41	3.60	3.66	4.51	5.19	7.73
K_2O	4.20	4.29	0.350	4.12	0.830	0.460	0.700	0.110
MgO	3.48	3.39	3.63	1.83	6.09	7.72	8.87	13.9
MnO	0.080	0.070	0.040	0.050	0.110	0.150	0.160	0.210
Na_2O	3.13	3.22	5.17	3.54	4.11	3.67	2.71	1.11
P_2O_5	0.400	0.400	0.420	0.240	0.400	0.370	0.390	0.260
TiO_2	0.700	0.690	0.710	0.490	0.570	0.540	0.550	0.500
LOI	0.730	1.05	1.24	1.45	3.27	3.98	4.80	6.53
Total	98.7	99.3	99.8	99.7	100	100	101	100
Parts per million								
Cr	54.2	52.3	58.9	22.7	31.9	20.5	26.3	31.6
Co	15.4	14.2	5.97	11.2	4.41	11.5	8.42	8.32
Ni	21.5	21.9	17.1	8.66	17.3	30.9	21.1	34.2
Rb	93.6	96.0	14.0	118	35.3	19.2	12.1	28.8
Sr	828	828	1045	942	525	535	108	402
Y	17.9	17.6	18.8	14.8	13.0	19.8	8.49	28.2
Nb	11.8	11.8	12.2	10.6	10.5	9.48	9.35	9.16
Ta	0.782	0.807	0.850	0.674	0.699	0.634	0.644	0.604
Ba	1853	1862	331	1368	561	393	70.4	550
Hf	3.35	2.96	3.06	4.47	3.28	2.73	2.23	2.96
Zr	142	133	139	196	84.7	265	175	278
La	38.0	41.6	53.7	34.3	25.6	42.3	16.0	47.0
Ce	71.0	76.1	96.0	58.2	50.4	77.0	30.3	76.3
Pr	8.08	8.65	10.9	6.65	5.90	9.22	3.35	9.88
Nd	29.2	30.6	37.5	22.9	21.6	33.5	11.8	36.3
Sm	5.61	5.54	6.44	3.81	3.80	6.10	2.16	6.37
Eu	1.37	1.39	1.75	1.07	0.743	1.29	0.417	1.29
Gd	4.30	4.26	4.63	2.84	2.59	4.65	1.47	5.56
Tb	0.666	0.677	0.692	0.436	0.428	0.754	0.266	0.855
Dy	3.19	3.07	3.33	2.38	2.24	3.51	1.35	4.37
Ho	0.630	0.586	0.623	0.455	0.430	0.680	0.289	0.858
Er	1.61	1.56	1.78	1.31	1.24	1.91	0.801	2.34
Tm	0.243	0.243	0.241	0.205	0.181	0.263	0.124	0.314
Yb	1.41	1.35	1.36	1.25	1.14	1.62	0.912	1.76
Lu	0.221	0.193	0.212	0.198	0.197	0.210	0.128	0.256
U	3.23	3.22	2.95	2.85	2.84	2.57	2.52	2.62
Th	13.1	13.6	13.7	11.2	12.0	10.5	9.47	11.2
Pb	14.5	12.8	6.82	12.5	11.1	22.0	16.7	35.2
Th/La	0.345	0.326	0.255	0.327	0.468	0.247	0.593	0.238
Sr/Y	46.4	47.1	55.6	63.6	40.4	27.1	12.8	14.2
La_N/Yb_N	19.4	22.1	28.3	19.6	16.1	18.7	12.6	19.2
Yb_N	8.27	7.94	7.99	7.38	6.71	9.56	5.36	10.3
Ba/Th	141	137	24.2	122	46.8	37.6	7.43	49.1
La_N/Sm_N	4.38	4.85	5.38	5.81	4.34	4.47	4.78	4.76
A/NK	1.51	1.50	1.72	1.53	1.96	2.21	2.71	7.07
A/CNK	0.800	0.805	0.734	1.06	1.67	1.77	1.97	5.08
Eu_N/Eu_N*	0.85	0.87	0.98	0.99	0.73	0.74	0.71	0.66
La/Yb	27.0	30.8	39.5	27.3	22.4	26.0	17.5	26.8
$Na_2O + K_2O$	7.33	7.51	5.52	7.66	4.94	4.13	3.41	1.22

A/NK = molar $Al_2O_3/(Na_2O + K_2O)$; A/CNK = molar $Al_2O_3/(Na_2O + K_2O + CaO)$; $Eu_N/Eu_N^* = Eu_N/ (Sm_N \times Gd_N)^{0.5}$

The subscript N denotes to be normarlized by chondrite values (Sun and McDonough 1989)

2003). Titanium-in-zircon temperatures (T_{Zr}; Fig. 12; ESM 2 Table A3) were calculated using the method of Ferry and Watson (2007). Because of the presence of quartz and titanite in the host intrusions, it is assumed that log a_{SiO2} = 1 and log a_{TiO2} = 0.7, respectively. The Pulang CQD zircon grains have T_{Zr} values of 700 ± 14 °C (range

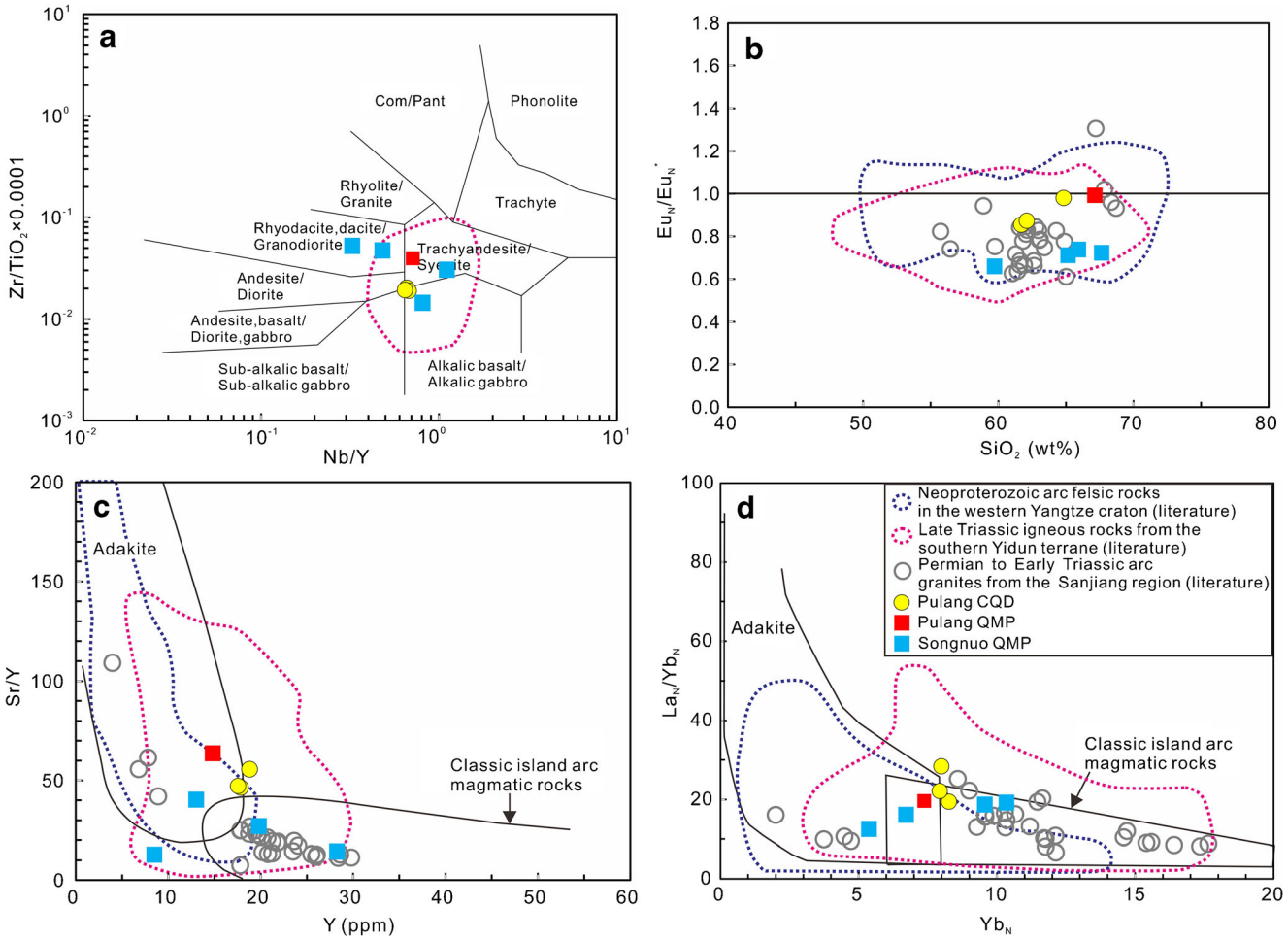

Fig. 9 Plots of (**a**) $Zr/TiO_2 \times 0.0001$ versus Nb/Y (Winchester and Floyd 1977), (**b**) Eu_N/Eu_N^* versus SiO_2 (wt%), (**c**) Sr/Y versus Y (ppm), and (**d**) La_N/Yb_N versus Yb_N for the Pulang and Songnuo porphyries. $Eu_N/Eu_N^* = Eu_N/(Sm_N \times Gd_N)^{0.5}$. Eu_N, Gd_N, La_N, Sm_N, and Yb_N are chondrite-normalized ratios. The normalization values are from Sun and McDonough (1989). Additional data for the Late Triassic igneous rocks in the southern Yidun terrane are from Wang et al. (2011), Leng et al. (2014, 2018), Cao et al. (2018), and Wang et al. (2018a). Data for the Permian to Early Triassic arc granites from the Sanjiang region are from Gao et al. (2010), Zi et al. (2012a, b), He et al. (2018), and Wang et al. (2018b). Data for the Neoproterozoic arc igneous rocks in the western Yangtze craton are from Zhao et al. (2018b). CQD coarse-grained quartz diorite porphyry, QMP quartz monzonite porphyry

= 675–721 °C, n = 19), with Eu_N/Eu_N^* values of 0.58 ± 0.03 (range = 0.54–0.64, n = 19). The Pulang syn-mineral QMP zircon grains have T_{Zr} values of 716 ± 10 °C (range = 700–729 °C, n = 13), with Eu_N/Eu_N^* values of 0.56 ± 0.03 (range = 0.52–0.61, n = 13). Zircon crystals from the Songnuo QMP have relatively high calculated temperatures and high Eu_N/Eu_N^* ratios (Fig. 12a), with T_{Zr} values of 725 ± 14 °C (range = 701–747 °C, n = 20), and Eu_N/Eu_N^* values of 0.62 ± 0.05 (range = 0.57–0.75, n = 20).

The Δ log fO_2 (FMQ) values estimated using the method of Loucks et al. (2020) are 1.59 ± 0.21 (range = 1.22–2.00, n = 19) for the Pulang CQD and 1.42 ± 0.16 (range = 1.19–1.67, n = 13) for the QMP (Fig. 12b). The Songnuo QMP has similar estimated Δ log fO_2 (FMQ) values of 1.75 ± 0.20 (range = 1.35–2.06, n = 20; Fig. 12b).

Discussion

Timing of porphyry intrusions and Cu-Au mineralization

In the Pulang porphyry Cu-Au deposit, the mineralization is predominantly associated with the QMP unit which is interpreted to be syn-mineralization (Fig. 4). The age of the QMP (215 ± 2 Ma) is within error of the published molybdenite Re-Os age of ~ 216 Ma and also consistent with the previous zircon U-Pb dating results (Li et al. 2011; Chen et al. 2014; Kong et al. 2016; Cao et al. 2019). The pre-mineral CQD was emplaced at 221 ± 2 Ma, which is in good agreement with the ID-TIMS (isotope dilution-thermal ionization mass spectrometry) zircon U-Pb ages (221 ± 1 Ma; Pang et al. 2009). Our work and previous dating results

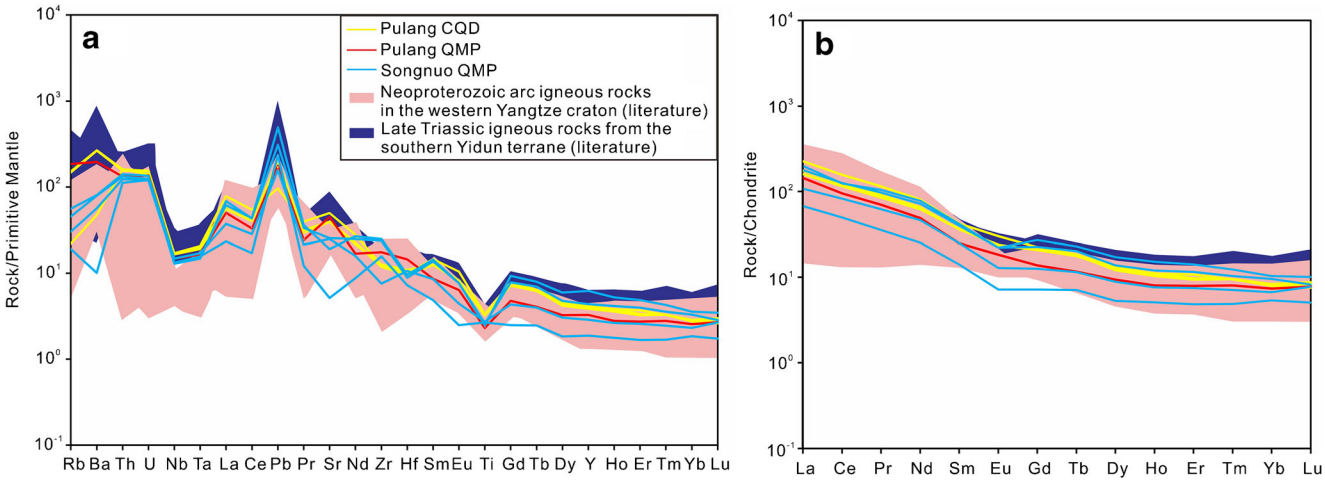

Fig. 10 **a** Primitive mantle-normalized trace element and **b** chondrite-normalized rare-earth element diagrams for the Pulang and Songnuo porphyries and the Neoproterozoic arc igneous rocks in the western Yangtze craton. The normalization values for the primitive mantle and chondrite are from Sun and McDonough (1989). Additional data for the Late Triassic igneous rocks in the southern Yidun terrane are from Wang et al. (2011), Leng et al. (2014, 2018), Cao et al. (2018), and Wang et al. (2018a). Data for the Neoproterozoic arc igneous rocks in the western Yangtze craton are from Zhao et al. (2007, 2018b), and Huang et al. (2009). CQD coarse-grained quartz diorite porphyry, QMP quartz monzonite porphyry

collectively define a ~ 6 m.y. span of magmatism for the Pulang complex. Ore formation occurred towards the end of the evolution of the Pulang intrusive complex, consistent with the observations in many other porphyry Cu deposits around the world (Richards et al. 2012; Chiaradia et al. 2013; Zhu et al. 2018).

For the Songnuo porphyry Cu deposit, the syn-mineral QMP was emplaced at 217 ± 2 Ma. The skarn alteration at Songnuo is associated with copper mineralization, thus the age of the garnet suggests that mineralization occurred at 223 ± 5 Ma, which is within error of the QMP zircon U-Pb age. In summary, the Pulang and Songnuo porphyry Cu-Au deposits in the southern Yidun terrane formed at ~ 216 Ma, representing a major pulse of mineralization in the region.

Magmatic oxidation state: key to porphyry Cu formation in the Sanjiang region

Magmatic oxidation state and water contents are two fundamental factors for the formation of porphyry Cu deposits (Burnham 1979; Candela 1992; Richards 2003; Loucks 2014). High magmatic water content is a vital component for magmatic-hydrothermal ore-forming systems (Richards 2011a). Magmatic redox state plays an important role in the speciation and solubility of sulfur in silicate melts, which in turn influences the solubility of chalcophile and siderophile elements (Hamlyn et al. 1985; Richards 2003, 2009, 2011b; Jugo 2009; Botcharnikov et al. 2011; Wang et al. 2014b). As mentioned above, in the Sanjiang region, the normal Paleo-

Table 2 Whole-rock Sr-Nd isotopic results for the Pulang and Songnuo porphyries

Sample no.	Rb (μg/g)	Sr (μg/g)	$^{87}Sr/^{86}Sr$	± σ	Sm (μg/g)	Nd (μg/g)	$^{143}Nd/^{144}Nd$	± 2σ	$(^{143}Nd/^{144}Nd)t$	$(^{87}Sr/^{86}Sr)i$	εNd (t = 216 Ma)	T_{DM1} (Ma)	T_{DM2} (Ma)
Pulang porphyry													
PLY-6	93.6	828	0.706621	0.000004	5.61	29.2	0.512414	0.000003	0.512251	0.705622	− 2.2	1152	1170
PLB17-8	96.0	828	0.706653	0.000003	5.54	30.6	0.512433	0.000002	0.512279	0.705629	− 1.6	1050	1125
PLB17-9	14.0	1045	0.705868	0.000004	6.44	37.5	0.512395	0.000002	0.512249	0.705750	− 2.2	1048	1172
PLY-8	117.8	942	0.706619	0.000003	3.81	22.9	0.512305	0.000003	0.512163	0.705514	− 3.9	1140	1308
Songnuo porphyry													
SN17-2	35.3	525	0.706981	0.000004	3.80	21.6	0.5123266	0.000002	0.512177	0.706386	− 3.6	1172	1287
SN17-3	19.2	535	0.706733	0.000004	6.10	33.5	0.5123282	0.000002	0.512174	0.706416	− 3.7	1209	1292
SN17-4	12.1	108	0.707078	0.000005	2.16	11.8	0.5123349	0.000002	0.512179	0.706093	− 3.6	1207	1283
SN17-9	28.8	402	0.707922	0.000004	6.37	36.3	0.5122922	0.000002	0.512143	0.707289	− 4.3	1217	1341

Rb, Sr, Sm, and Nd concentrations are from Table 1; $T_{DM1} = (1/\lambda) \times Ln[((^{143}Nd/^{144}Nd)_{sample} - (^{143}Nd/^{144}Nd)_{DM})/((^{147}Sm/^{144}Nd)_{sample} - (^{147}Sm/^{144}Nd)_{DM} + 1)]$ and $T_{DM2} = T_{DM1} - (T_{DM1} - t) \times ((f_{cc} - f_s)/(f_{cc} - f_{DM}))$ calculation for T_{DM2} following assuming of Keto and Jacobsen (1987) where $f_{cc} = -0.4$, $f_{DM} = 0.0859$. See text for the $^{143}Nd/^{144}Nd$ and $^{147}Sm/^{144}Nd$ values of present day chondrite and depleted mantle; see Table A1 for sample locations

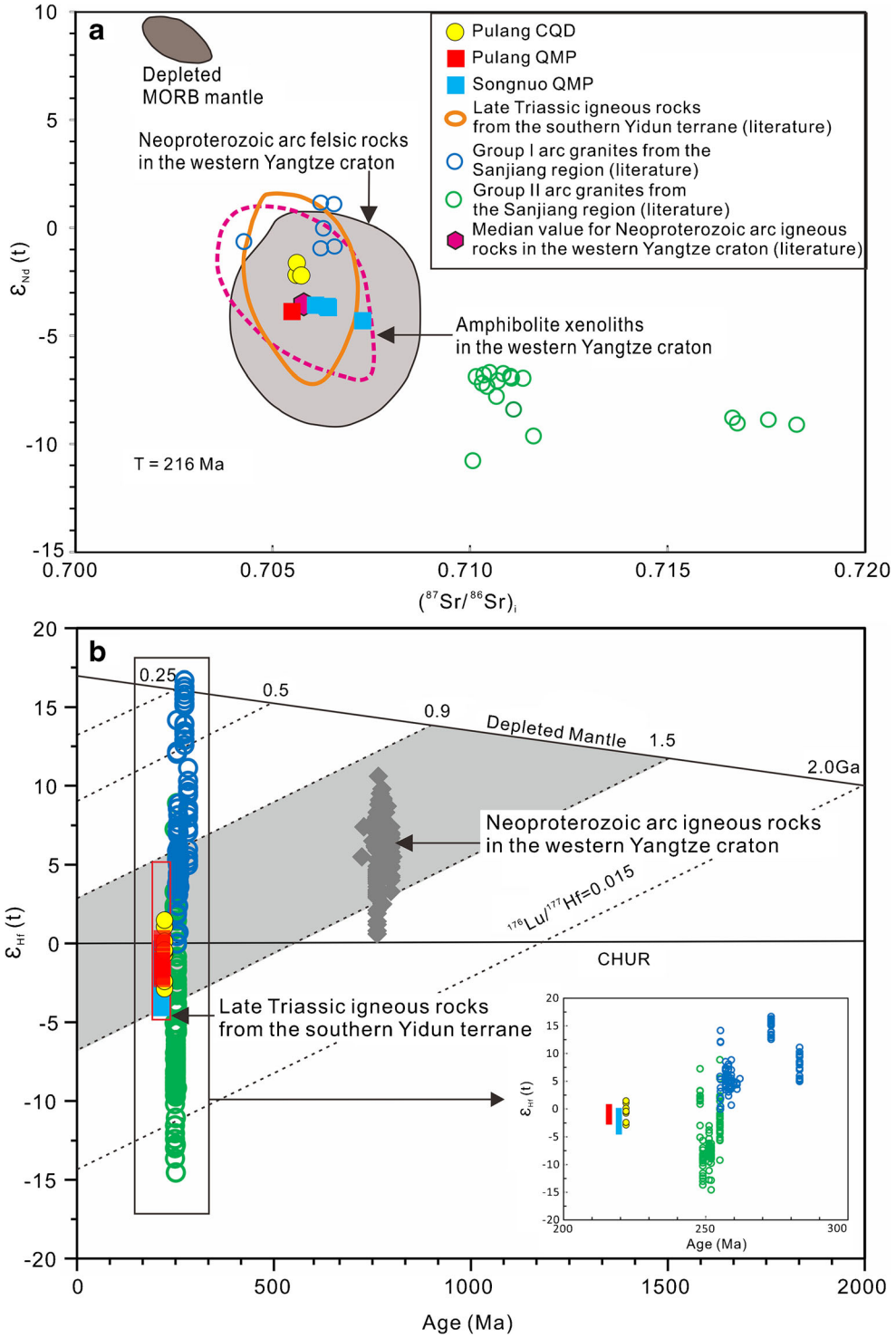

Fig. 11 **a** ε_{Nd} (t) versus initial $^{87}Sr/^{86}Sr$ ratios for the Pulang and Songnuo porphyries, Late Triassic igneous rocks in the southern Yidun terrane, and the Neoproterozoic arc igneous rocks in the western Yangtze craton, calculated at t = 216 Ma. **b** ε_{Hf} (t) values versus U-Pb ages of zircon grains from the Pulang and Songnuo porphyries, Late Triassic igneous rocks in the southern Yidun terrane, and the Neoproterozoic arc igneous rocks in the western Yangtze craton. The field of depleted MORB mantle is after Pilet et al. (2011). The field of amphibolite xenoliths in the western Yangtze craton is after Zhao et al. (2004), Hou et al. (2017), and Zhou et al. (2017). In figure (**a**), data are after Gao et al. (2010), Wu et al. (2013), and Wang et al. (2018b) for the group I arc granites from the Sanjiang region, after Zi et al. (2012a), Liu et al. (2015, 2020), and He et al. (2018) for the group II arc granites, after Wang et al. (2011), Leng et al. (2014), and Chen et al. (2014) for the Late Triassic igneous rocks in the southern Yidun terrane, and after Zhao et al. (2018b) for the Neoproterozoic arc igneous rocks in the western Yangtze craton. In figure (**b**), data are after Yang et al. (2011), Zi et al. (2012b), Liu et al. (2018), and Wang et al. (2018b) for the group I arc granites from the Sanjiang region, after Zi et al. (2012a), Li et al. (2013a), Liu et al. (2015), and He et al. (2018) for the group II arc granites, after Leng et al. (2018), Cao et al. (2018), Wang et al. (2018a), and Yang et al. (2018) for the Late Triassic igneous rocks in the southern Yidun terrane, and after Zhao et al. (2018b) for the Neoproterozoic arc igneous rocks in the western Yangtze craton. CQD coarse-grained quartz diorite porphyry, QMP quartz monzonite porphyry

Table 3 In situ zircon Hf isotope compostions for the Pulang and Songnuo porphyries

Spot no.	$^{176}Hf/^{177}Hf$	1σ	$^{176}Lu/^{177}Hf$	1σ	$^{176}Yb/^{177}Hf$	1σ	Age (Ma)	$\varepsilon_{Hf}(t)$	T_{DM1} (Ma)	T_{DM2} (Ma)
PLY-6 - 1	0.282568	0.000012	0.000889	0.000004	0.025728	0.000160	221.0	− 2.46	965	1408
PLY-6 - 2	0.282555	0.000011	0.000534	0.000005	0.015442	0.000150	221.0	− 2.89	975	1435
PLY-6 - 3	0.282569	0.000011	0.000605	0.000004	0.017701	0.000140	221.0	− 2.41	957	1404
PLY-6 - 4	0.282667	0.000011	0.000800	0.000002	0.023187	0.000043	221.0	1.04	824	1187
PLY-6 - 5	0.282621	0.000011	0.000863	0.000001	0.024356	0.000061	221.0	− 0.580	890	1289
PLY-6 - 6	0.282617	0.000012	0.000660	0.000001	0.019112	0.000013	221.0	− 0.692	891	1296
PLY-6 - 7	0.282617	0.000011	0.000903	0.000002	0.025659	0.000087	221.0	− 0.745	897	1299
PLY-6 - 8	0.282679	0.000012	0.000957	0.000001	0.028016	0.000046	221.0	1.45	811	1161
PLY-6 - 9	0.282640	0.000011	0.000556	0.000001	0.016254	0.000038	221.0	0.109	857	1246
PLY-6 - 10	0.282625	0.000010	0.000793	0.000001	0.023135	0.000023	221.0	− 0.449	883	1281
PLY-6 - 11	0.282623	0.000011	0.000711	0.000003	0.020407	0.000068	221.0	− 0.508	884	1285
PLY-6 - 12	0.282626	0.000012	0.001113	0.000005	0.033046	0.000220	221.0	− 0.443	889	1280
PL17-8 - 1	0.282597	0.000010	0.000706	0.000001	0.020864	0.000031	215.1	− 1.54	920	1345
PL17-8 - 3	0.282649	0.000011	0.000683	0.000001	0.021268	0.000075	215.1	0.294	847	1229
PL17-8 - 4	0.282609	0.000010	0.000678	0.000001	0.019508	0.000025	215.1	− 1.12	903	1319
PL17-8 - 5	0.282596	0.000010	0.000601	0.000001	0.018257	0.000049	215.1	− 1.58	919	1347
PL17-8 - 6	0.282593	0.000012	0.000674	0.000003	0.019625	0.000069	215.1	− 1.69	925	1354
PL17-8 - 7	0.282578	0.000011	0.000976	0.000001	0.028350	0.000023	215.1	− 2.26	953	1390
PL17-8 - 8	0.282581	0.000010	0.000647	0.000001	0.019583	0.000055	215.1	− 2.11	941	1381
PL17-8 - 9	0.282609	0.000011	0.000718	0.000001	0.021210	0.000062	215.1	− 1.12	903	1319
PL17-8 - 12	0.282642	0.000011	0.000765	0.000001	0.022959	0.000018	215.1	0.027	859	1246
PL17-8 - 13	0.282617	0.000011	0.000702	0.000003	0.021039	0.000100	215.1	− 0.831	892	1300
SN17-4-1	0.282537	0.000014	0.001038	0.000003	0.035065	0.000130	216.5	− 3.64	1012	1480
SN17-4-2	0.282584	0.000013	0.001021	0.000004	0.034758	0.000089	216.5	− 1.97	946	1375
SN17-4-3	0.282573	0.000014	0.001043	0.000004	0.036537	0.000190	216.5	− 2.36	962	1400
SN17-4-4	0.282598	0.000011	0.000865	0.000004	0.029683	0.000150	216.5	− 1.47	923	1343
SN17-4-5	0.282580	0.000014	0.000956	0.000011	0.034017	0.000430	216.5	− 2.11	950	1384
SN17-4-6	0.282589	0.000013	0.000888	0.000007	0.031149	0.000300	216.5	− 1.79	936	1363
SN17-4-7	0.282612	0.000012	0.001100	0.000009	0.038121	0.000210	216.5	− 0.990	908	1313
SN17-4-8	0.282583	0.000013	0.000975	0.000006	0.033910	0.000270	216.5	− 2.00	946	1377
SN17-4-9	0.282613	0.000014	0.001080	0.000004	0.037911	0.000055	216.5	− 0.970	907	1312
SN17-4-10	0.282566	0.000013	0.001060	0.000003	0.037785	0.000150	216.5	− 2.62	972	1416
SN17-4-11	0.282569	0.000013	0.000788	0.000001	0.026567	0.000024	216.5	− 2.49	962	1408
SN17-4-12	0.282533	0.000014	0.001344	0.000013	0.047073	0.000450	216.5	− 3.83	1027	1492
SN17-4-13	0.282550	0.000012	0.000923	0.000002	0.033288	0.000040	216.5	− 3.16	991	1450
SN17-4-14	0.282527	0.000013	0.001146	0.000006	0.041727	0.000190	216.5	− 4.01	1029	1503
SN17-4-15	0.282526	0.000014	0.001073	0.000008	0.036402	0.000400	216.5	− 4.05	1030	1506
SN17-4-16	0.282543	0.000013	0.001104	0.000008	0.039712	0.000240	216.5	− 3.45	1006	1468
SN17-4-17	0.282556	0.000014	0.000916	0.000006	0.031033	0.000190	216.5	− 2.94	982	1436
SN17-4-18	0.282550	0.000012	0.001043	0.000004	0.036068	0.000200	216.5	− 3.18	994	1451
SN17-4-19	0.282569	0.000014	0.000938	0.000011	0.033143	0.000420	216.5	− 2.50	965	1408
SN17-4-20	0.282553	0.000013	0.000837	0.000006	0.029974	0.000220	216.5	− 3.03	984	1442
SN17-4-21	0.282551	0.000013	0.001039	0.000001	0.035993	0.000091	216.5	− 3.16	993	1450
SN17-4-22	0.282581	0.000013	0.000625	0.000004	0.021704	0.000150	216.5	− 2.02	940	1378
SN17-4-23	0.282570	0.000013	0.001169	0.000004	0.040208	0.000120	216.5	− 2.49	969	1407
SN17-4-24	0.282528	0.000011	0.000956	0.000003	0.035505	0.000062	216.5	− 3.96	1024	1500
SN17-4-25	0.282628	0.000013	0.000870	0.000002	0.030379	0.000085	216.5	− 0.401	881	1276
Standards										
Penglai	0.282906	0.000016	0.000332	0.000001	0.011620	0.000016				
Penglai	0.282896	0.000016	0.000334	0.000001	0.011754	0.000028				
Penglai	0.282929	0.000015	0.000334	0.000001	0.011627	0.000022				
Penglai	0.282908	0.000015	0.000329	0.000001	0.012431	0.000034				
Penglai	0.282892	0.000013	0.000332	0.000001	0.012444	0.000015				
Penglai	0.282877	0.000015	0.000332	0.000001	0.012404	0.000019				
Penglai	0.282952	0.000015	0.000337	0.000001	0.012990	0.000027				
Penglai	0.282907	0.000016	0.000326	0.000000	0.012236	0.000035				

Age results, see Table A2; $T_{DM1} = (1/\lambda) \times Ln[(({}^{176}Hf/{}^{177}Hf)_{sample} - {}^{176}Hf/{}^{177}Hf)_{DM})/(({}^{176}Lu/{}^{177}Hf)_{sample} - ({}^{176}Lu/{}^{177}Hf)_{DM} + 1)]$. See text for the $^{177}Hf/^{176}Hf$ and $^{177}Lu/^{176}Hf$ values of present day chondrite and depleted mantle

Tethyan arc igneous rocks (e.g., the Jiangda–Weixi Arc belt) are not associated with significant mineralization, with porphyry Cu deposits only occurring in the southern Yidun terrane (Fig. 1). Here, we attempt to explain the difference in metallogeny by examining magmatic water contents and oxygen fugacity.

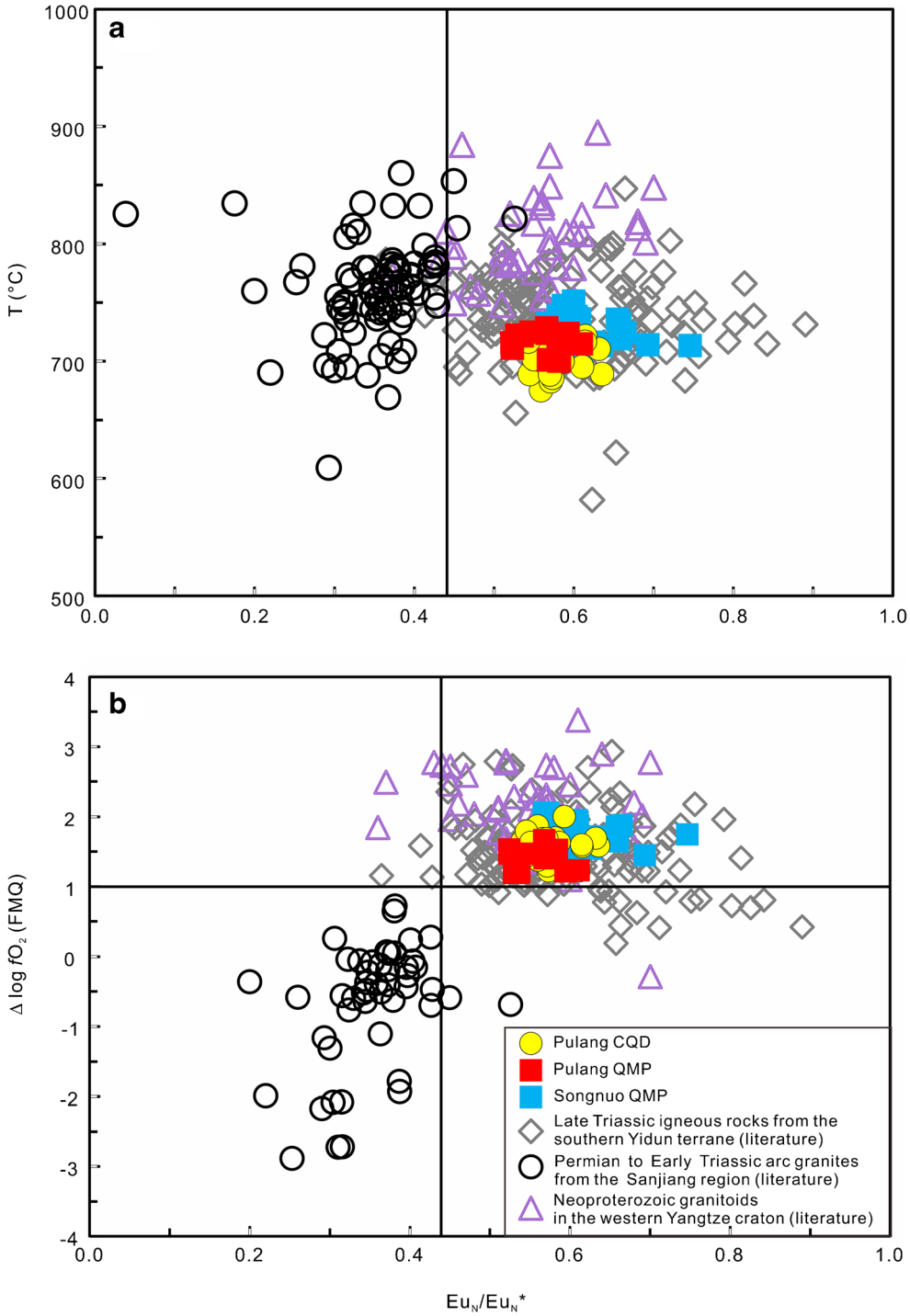

Fig. 12 Plots of (**a**) Zircon Eu_N/Eu_N^* versus temperature, and (b) Zircon Eu_N/Eu_N^* versus Δ log fO_2 (FMQ). Eu_N/Eu_N^* is the europium anomaly, calculated as $Eu_N/Eu_N^* = Eu_N/(Sm_N \times Gd_N)^{0.5}$, using the chondrite normalization values of Sun and McDonough (1989). Temperatures calculated using the Ti-in-zircon thermometer of Ferry and Watson (2007): log (ppm Ti-in-zircon) = (5.711 ± 0.072) - (4800 ± 86)/T (K) - log a_{SiO2} + log a_{TiO2}, wherein log a_{SiO2} is assumed to be 1 because of the presence of quartz, and log a_{TiO2} = 0.7 due to the presence of titanite. Data for the Neoproterozoic granitoids are from Meng et al. (2015). Data for the Permian to Early Triassic arc granitoids are from Li et al. (2013a), and Wang et al. (2020b). Data for the Late Triassic igneous rocks in the southern Yidun terrane are after Jin et al. (2013), Kong et al. (2016), Meng et al. (2018), and Li et al. (2019b). CQD coarse-grained quartz diorite porphyry, QMP quartz monzonite porphyry

A number of lines of evidence suggest that the causative magmas for the Pulang and Songnuo porphyries were water-rich, including (1) the presence of abundant amphibole and biotite phenocrysts, indicating at least 4 wt% H_2O in melts (ESM 1 Figs. 1d, f; Burnham 1979; Naney 1983; Ridolfi et al. 2010; Richards 2011a), and (2) estimates of melt water content from high-Al amphibole compositions giving values between 4.8 and 6.2 wt% (Leng et al. 2018). The magmas have relatively high whole-rock Sr/Y ratios (38.4 ± 19; n = 8) with minor or no negative Eu anomalies (Eu_N/Eu_N^* = 0.82 ± 0.13, n = 8). These features reflect hydrous magmas with no early plagioclase crystallization but abundant amphibole fractionation (Green and Pearson 1985; Moore and Carmichael 1998; Richards and Kerrich 2007). Considering that the Late Triassic igneous rocks in the southern Yidun terrane share similar petrological and geochemical features with the

Pulang and Songnuo porphyries (Figs. 9 and 10; Reid et al. 2007; Wang et al. 2011; Chen et al. 2014), it is suggested they were all derived from hydrous magmas. The Permian to Early Triassic granites from the Jiangda–Weixi Arc belt also show small Eu negative anomalies (Eu_N/Eu_N^* = 0.8 ± 0.1, n = 29) and relatively high whole-rock Sr/Y ratios (24.5 ± 20, n = 29) (Fig. 9b, c; Gao et al. 2010; Zi et al. 2012a, b; He et al. 2018; Wang et al. 2018b). Given the presence of phenocrysts of amphibole and biotite in the Permian to Early Triassic arc granites (Zi et al. 2012a; Wang et al. 2018b), they also likely formed from hydrous melts (Wang et al. 2014c). In summary, the generative magmas related to the Late Triassic igneous rocks from the southern Yidun terrane and the Permian to Early Triassic arc granites are both rich in water. Therefore, the water content of magma is not the key control on distribution of porphyry Cu deposits within the Sanjiang region.

Zircon compositions have been widely used to estimate magmatic oxidation state (Ballard et al. 2002; Liang et al. 2006; Dilles et al. 2015; Loucks et al. 2018; Zhu et al. 2018). For example, the zircon Ce^{4+}/Ce^{3+} or Ce/Ce^* ratio has been widely used as a proxy for magmatic oxygen fugacity (Ballard et al. 2002; Trail et al. 2012; Smythe and Brenan 2015, 2016). However, it is difficult to estimate the Ce^{4+}/Ce^{3+} ratio due to a number of issues and it often yields extremely high or low $\Delta \log fO_2$ (FMQ) values (− 8 to + 10; Dilles et al. 2015; Lu et al. 2016; Lee et al. 2017; Loader et al. 2017; Zhu et al. 2018; Zou et al. 2019; Rezeau et al. 2019). There is a modified Ce-in-zircon oxybarometer (Smythe and Brenan 2016) based on Ti-in-zircon thermometers and H_2O contents in melts. However, accurate H_2O contents of magmas during zircon crystallization are hard to obtain (Li et al. 2019b; Zou et al. 2019).

Europium is preferably partitioned into zircon as Eu^{3+} in oxidized magmas (Ballard et al. 2002; Hoskin and Schaltegger 2003), whereas in hydrous magma, suppression of plagioclase crystallization also leads to small Eu negative anomalies. As suggested by Dilles et al. (2015) and Lu et al. (2016), relatively high zircon Eu_N/Eu_N^* ratios (> 0.3 or 0.4) cannot be attributed solely to suppression of plagioclase fractionation, and thus can be used as an indicator of relatively high magmatic oxidation states or water contents in melts. Zircon samples from porphyry rocks in the southern Yidun terrane (including Pulang and Songnuo porphyries, and other Late Triassic igneous rocks) show higher Eu_N/Eu_N^* ratios (> 0.44) than published data for Permian to Early Triassic arc intrusions (Eu_N/Eu_N^* mostly < 0.44; Fig. 12). Considering the two groups of igneous rocks were both derived from hydrous magmas, it suggests that the magmas associated with porphyry rocks in the southern Yidun terrane were more oxidized than the Permian to Early Triassic arc suites.

Recently, Loucks et al. (2020) derived a novel method for determining the oxidation state of a magma as zircon crystallized using Ce, U, and Ti in zircon that yields results with a standard error of ± 0.6 log unit fO_2. Using this method, the causative magmas for the Pulang and Songnuo porphyry rocks yielded $\Delta \log fO_2$ (FMQ) values of 1.61 ± 0.23 (n = 52), significantly higher than those of the Permian to Early Triassic granites in the Sanjiang region with $\Delta \log fO_2$ (FMQ) values of − 0.68 ± 0.88 (n = 48), which were recalculated using the published zircon compositions (Fig. 12b; Li et al. 2013a; Wang et al. 2020b). Our results for the Pulang porphyry are similar to previous studies but show a smaller range of log fO_2 values (Meng et al. 2018; Li et al. 2019b). The recalculated results for the other Late Triassic porphyries in the southern Yidun terrane are indistinguishable from the Pulang and Songnuo porphyries (Fig. 12b; Jin et al. 2013; Kong et al. 2016; Meng et al. 2018; Li et al. 2019b). Given the positive correlation between zircon Eu_N/Eu_N^* ratios and $\Delta \log fO_2$ (FMQ) values (Fig. 12b), we suggest that the Pulang and Songnuo porphyries and Late Triassic igneous rocks in the southern Yidun terrane have been derived from moderately oxidized magmas ($\Delta \log fO_2$ (FMQ) > 1), whereas the Permian–Early Triassic arc granitoids were generated under a relatively reduced conditions ($\Delta \log fO_2$ (FMQ) < 0). The reduced magmas would promote sulfide saturation and strip Cu and Au from the melt, detrimental to porphyry Cu-Au formation (Richards 2011a, b; Richards and Şengör 2017; Sun et al. 2017). In contrast, sulfide saturation was less likely to occur under relatively oxidized conditions, and thus the Late Triassic suites in the southern Yidun terrane are likely to be more prospective for the generation of porphyry Cu-Au deposits (Fig. 12; Meng et al. 2018).

Petrogenesis and origin of oxidized magmas

It is widely believed that the Late Triassic igneous rocks (including the Pulang and Songnuo porphyries) from the southern Yidun terrane were derived from partial melting of the metasomatized asthenospheric mantle wedge, similar to the normal Paleo-Tethyan arc igneous rocks (Permian to Early Triassic) in the Sanjiang region (Fig. 1; Hou et al. 1993; Reid et al. 2007; Roger et al. 2010; Wang et al. 2011; Deng et al. 2014; Yang et al. 2017; Leng et al. 2018). It has been proposed that these magmas formed from reworking of juvenile lower crust, like the Late Triassic granitoids within the Songpan–Garzê terrane to the east (Fig. 1; Zhang et al. 2006; Zhang et al. 2014; Peng et al. 2014).

The Pulang and Songnuo porphyry rocks show arc-like features characterized by high LILE and low HFSE abundances, and are indistinguishable from the Neoproterozoic arc igneous rocks in the western Yangtze craton (Fig. 10; Zhao and Zhou 2007; Huang et al. 2009; Zhao et al. 2018b). As mentioned earlier, there are Neoproterozoic magmatic rocks (meta-rhyolite) in the southern Yidun terrane (Fig. 2), consistent with this region sharing a common Neoproterozoic basement with the western Yangtze craton (Tian et al. 2020).

The Pulang and Songnuo porphyries show $(^{87}Sr/^{86}Sr)_i$ of 0.7055–0.7073 and $\varepsilon_{Nd}(t)$ ratios from − 4.3 to − 1.6 similar to the Neoproterozoic arc rocks and amphibolite xenoliths in the western Yangtze craton (Fig. 11a; Zhao et al. 2018b). The amphibolite xenoliths have been interpreted to represent the Neoproterozoic arc root or juvenile lower crust in the western Yangtze craton, which formed as a result of Neoproterozoic oceanic subduction (Zhao et al. 2004; Hou et al. 2017; Zhou et al. 2017). The Sr-Nd isotopic features of the Pulang and Songnuo rocks are different from the Permian to Early Triassic granites from the Jiangda–Weixi, Yunxian, and Yaxianqiao belts to the west which are typical arc igneous rocks related to the normal Paleo-Tethyan subduction (Figs. 1 and 11a; Zi et al. 2012a; Wu et al. 2013; Liu et al. 2015, 2020; He et al. 2018; Wang et al. 2018b). The Permian to Early Triassic arc granites can be divided into two groups based on their isotope compositions. Group I formed during the Early to Middle Permian and have $(^{87}Sr/^{86}Sr)_i$ ratios of 0.7043 to 0.7066 and $\varepsilon_{Nd}(t)$ values of − 0.9 to 1.6, indicative of more depleted magma source than the Pulang and Songnuo porphyry rocks (Fig. 11a; Gao et al. 2010; Wu et al. 2013; Wang et al. 2018b). Conversely, group II was emplaced between the latest Permian to Early Triassic and shows more enriched Sr-Nd isotopic compositions than the Pulang and Songnuo samples [$(^{87}Sr/^{86}Sr)_i$ = 0.7092–0.7183; $\varepsilon_{Nd}(t)$ = − 11 to − 6; Fig. 11a; Zi et al. 2012a; Liu et al. 2015, 2020; He et al. 2018]. In terms of zircon Hf isotopes, the Pulang and Songnuo rocks plot along the trend of Hf isotope evolution for the Neoproterozoic arc rocks, whereas both groups from the Permian to Early Triassic arc granites samples fall outside that field (Fig. 11b; Zhao et al. 2018b; Yang et al. 2011; Zi et al. 2012a; Li et al. 2013a; He et al. 2018; Wang et al. 2018b; Liu et al. 2018). The group I and II rocks from the Permian to Early Triassic arc granites show more primitive and evolved zircon Hf isotopic compositions than those of Pulang and Songnuo porphyries, respectively (Group I: $\varepsilon_{Hf}(t)$ = mostly 0–+ 15; Group II: $\varepsilon_{Hf}(t)$ = mostly − 15–0; Fig. 11b; Yang et al. 2011; Zi et al. 2012a, b; Li et al. 2013a; Liu et al. 2015, 2018; He et al. 2018; Wang et al. 2018b). Collectively, the Pulang and Songnuo rocks are geochemically distinct from the Permian to Early Triassic arc granites in the Sanjiang region but identical to the Neoproterozoic arc igneous rocks in the western Yangtze craton. Consequently, we propose that the Pulang and Songnuo rocks were likely derived not from the subduction of the Paleo-Tethyan Ocean but from partial melting of the Neoproterozoic arc root. For the Permian to Early Triassic arc granites in the Sanjiang region, they might be derived from partial melting of the mantle wedge, which mixed with variable degree of crustal melts (e.g., Zi et al. 2012a; Liu et al. 2015; He et al. 2018; Wang et al. 2018b).

Late Triassic igneous rocks coeval with the Pulang and Songnuo porphyries are widespread in the southern Yidun terrane (Fig. 2). From the published data, these Late Triassic igneous rocks have geochemical compositions similar to the Pulang and Songnuo porphyries (Figs. 9, 10, and 11; Reid et al. 2007; Wang et al. 2011; Chen et al. 2014). They have relatively homogeneous Sr-Nd-Hf isotope values [$(^{87}Sr/^{86}Sr)_i$ = 0.7050–0.7060; $\varepsilon_{Nd}(t)$ = − 5.0–+ 1.0, $\varepsilon_{Hf}(t)$ = − 5.00–+ 5.00; Fig. 11; Wang et al. 2011; Leng et al. 2012, 2018; Cao et al. 2018; Wang et al. 2018a; Yang et al. 2018], that broadly overlap with the Pulang and Songnuo porphyries as well as the Neoproterozoic igneous rocks in the western Yangtze craton. But, they are distinct from the Permian to Early Triassic arc igneous rocks in the Sanjiang region (Fig. 11). In addition, a number of inherited zircon grains with Neoproterozoic ages have been reported in the Late Triassic igneous rocks (e.g., Leng et al. 2014). Therefore, we hypothesize that the Late Triassic igneous rocks from the southern Yidun terrane might have a common magma source similar to that of the Pulang and Songnuo porphyries, derived from partial melting of the Neoproterozoic arc root.

The most recent geological and paleomagnetic studies combined with tectonic reconstructions suggest that the Paleo-Tethys Ocean closed prior to ~ 220 Ma, before the emplacement of the ~ 216 Ma magmatic rocks in the southern Yidun terrane (Wang et al. 2018c; Zhao et al. 2018a; Huang et al. 2018; Li et al. 2019a; Yan et al. 2019). Consequently, these Late Triassic igneous rocks cannot be directly related to active subduction but formed in a post subduction setting. It is possible that they might be products of subduction of the Paleo-Tethyan branch (i.e., the so-called Garzê–Litang Ocean), associated with a series of thrust fault systems. However, these compressional fault systems generally have Cenozoic ages and formed along pre-existing weaknesses (Sun et al. 2018). The presence of shallow-water facies glauconite and carbonate rocks in the ophiolite-like complex in the Garzê–Litang suture zone argues against the presence of a mature ocean basin (Liu et al. 1994; Zhang et al. 1998), as does the presence of the Emeishan flood basalts on both sides of the Ganzi–Litang suture (~ 260 Ma; Song et al. 2004; Xiao et al. 2005; Xu et al. 2008). Furthermore, the Yidun terrane and the eastern Songpan−Ganzi terrane were adjacent to each other by the Middle Triassic, before the emplacement of the ~ 216 Ma magmatic rocks, as turbidites within the terranes display similar zircon age spectra (Jian et al. 2019). Consequently, rather than the Garzê–Litang suture representing the closure of a mature ocean, it was likely either a small basin or continental rifted margin, with no slab subduction. A slab break-off model has been proposed to have triggered upwelling of asthenospheric mantle that in turn caused partial melting of the previous arc root (Fig. 13). This is supported by the occurrence of ~ 216 Ma E-MORB-like basalts in the southern Yidun terrane (Fig. 2; Chen et al. 2017). Taken together, partial melting of the residue of a previous (Neoproterozoic) arc root triggered by slab break-off

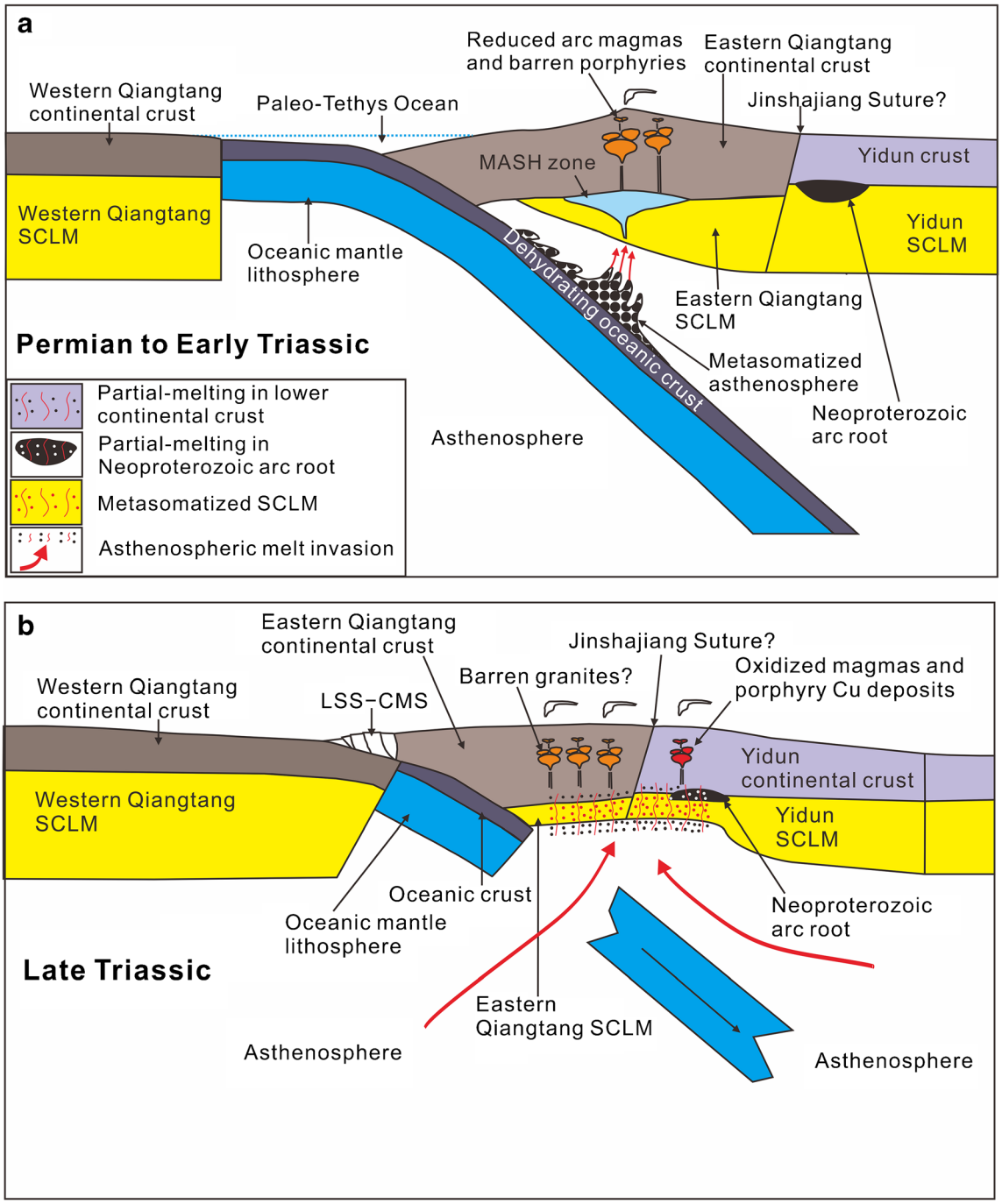

Fig. 13 Schematic cross sections illustrating the proposed petrogenesis of Permian to Early Triassic Paleo-Tethyan arc belt and Late Triassic igneous rocks in the southern Yidun terrane. **a** Permian to early Triassic magmatism was triggered by normal subduction of the Paleo-Tethys Ocean and formed by partial melting of the hydrated mantle wedge and lower continental crust (MASH = melting, assimilation, storage, and homogenization; Hildreth and Moorbath 1988). **b** Late Triassic magmatism in the southern Yidun terrane was triggered by slab breakoff and upwelling of asthenospheric melts and partial melting of the Neoproterozoic arc root. The generative magmas inherited relatively oxidized and hydrous features of the Neoproterozoic arc root and therefore were fertile for porphyry Cu formation in the upper crust. LSS–CMS Longmu Tso-Shuanghu–Changning-Mengliang suture, SCLM subcontinental lithospheric mantle

resulted in Late Triassic magmatism in the southern Yidun terrane with geochemical and isotopic features similar to the Neoproterozoic arc igneous rocks.

As the Neoproterozoic arc magmas were water-rich and relatively oxidized, based on the high whole-rock Sr/Y ratios and $\Delta \log fO_2$ (FMQ) values (2.14 ± 0.60, $n = 43$; e.g., Meng et al. 2015; Yao et al. 2018; Zhao et al. 2018b), we suggest that the Pulang and Songnuo porphyries, and Late Triassic igneous rocks in the southern Yidun terrane inherited the high magmatic oxygen fugacity and water contents of the

Neoproterozoic arc root. The relatively oxidized magmas could facilitate the remobilization of residual sulfides from Neoproterozic arc magmas, leading to magmatic-hydrothermal mineralization in the upper crust (Richards 2009; Wilkinson 2013; Chiaradia 2014; Hou et al. 2017). In summary, the Permian to Early Triassic arc magmas in the Sanjiang region were associated with normal subduction of the Paleo-Tethys Ocean and formed by partial melting of a hydrated mantle wedge (Fig. 13a). These magmas were relatively reduced and thus infertile for porphyry copper mineralization. After the closure of the Paleo-Tethys Ocean, slab break-off at ~ 216 Ma triggered upwelling of asthenospheric mantle and subsequent partial melting of the Neoproterozoic arc root in the southern Yidun terrane (Fig. 13b; Kay and Mpodozis 2001; Richards 2009). The generative magmas were relatively oxidized and hydrous, almost indistinguishable from the Neoproterozoic arc magmatism and fertile for porphyry Cu formation. It is noteworthy that there are voluminous Late Triassic igneous rocks in the Eastern Qiangtang terrane (Figs. 1 and 13b). However, they were probably not derived from the Neoproterozoic arc root but from more ancient lower crust (e.g., Peng et al. 2014, 2015; Wang et al. 2014a; Wang et al. 2018b; Li et al. 2019a). It is likely that their generative magmas were relatively reduced and thus infertile for porphyry Cu formation. However, further work is necessary including accurate estimates of the magmatic oxidation state of this Late Triassic magmatism.

Conclusions

Zircon U-Pb ages indicate that the Pulang porphyry complex was emplaced over ~ 6 m.y. (221 ± 2 Ma and 215 ± 2 Ma). The Songnuo porphyry formed at 217 ± 2 Ma, roughly consistent with the garnet U-Pb age from the skarn (223 ± 5 Ma). The two porphyry Cu-Au deposits might represent a significant pulse of mineralization in the southern Yidun terrane. Based on the geochemical compositions of the Pulang and Songnuo porphyries in the southern Yidun terrane, we suggest that the causative magmas were relatively oxidized and therefore fertile for porphyry Cu deposits formation. In contrast, the normal Paleo-Tethyan arc magmas were reduced and thus largely ore-barren. As the Pulang and Songnuo porphyries and Late Triassic igneous rocks in the southern Yidun terrane have Sr-Nd-Hf isotope compositions and magmatic oxygen fugacities identical to the nearby Neoproterozoic arc rocks, it is suggested that they might be derived from partial melting of that root. As the most recent tectonic reconstructions suggest that the Paleo-Tethys Ocean closed before ~220 Ma, we propose that the Pulang and Songnuo porphyry Cu-Au deposits formed in a postsubduction setting. Our results are consistent with the Paleo-Tethyan arc magmas being reduced and broadly infertile for porphyry Cu formation. However, Neoproterozoic subduction had generated an oxidized, fertile arc column that was reactivated to form the Pulang and Songnuo porphyries, and Late Triassic igneous rocks in the southern Yidun terrane.

Supplementary Information The online version contains supplementary material available at https://doi.org/10.1007/s00126-021-01049-0.

Acknowledgements Thanks to Dr. Jian-Feng Gao from the Institute of Geochemistry, Chinese Academy of Sciences for the constructive comments on an early version of this manuscript. Jing-Jing Zhu thanks Prof. Jeremy Richards, who was Jing-Jing's post-doctoral supervisor and passed away in June of 2019. Jeremy encouraged Jing-Jing to write this contribution when they were working at Laurentian University, Canada, and we dedicate this paper to his memory. We thank Prof. Bernd Lehmann and two anonymous reviewers for their constructive comments on this manuscript.

Funding This work was jointly funded by the National Natural Science Foundation of China (91955209), the project of "Innovative Team of One Belt and One Road" of the Chinese Academy of Sciences, the Strategic Priority Research Program (XDB18000000), Hundred Talent Plan of the Chinese Academy of Sciences to Jing-Jing Zhu, the National Key Research and Development Program of China (2016YFC0600503), the National Natural Science Foundation of China (41673049, 42073047), and the project under the Frontier Programme of the State Key Laboratory of Ore Deposit Geochemistry.

Declarations

Competing interests The authors declare no competing interests.

References

Ballard JR, Palin MJ, Campbell IH (2002) Relative oxidation states of magmas inferred from $Ce^{(IV)}/Ce^{(III)}$ in zircon: application to porphyry copper deposits of northern Chile. Contrib Mineral Petrol 144: 347–364. https://doi.org/10.1007/s00410-002-0402-5

BGMRSP <Bureau of Geology and Mineral Resources of Sichuan Province> (1991) Regional geology of Sichuan Province. Geological Publishing House, Beijing (in Chinese with English summary)

Blichert Toft J, Albarède F (1997) The Lu-Hf isotope geochemistry of chondrites and the evolution of the mantle-crust system. Earth Planet Sci Lett 148:243–258

Botcharnikov RE, Linnen RL, Wilke M, Holtz F, Jugo PJ, Berndt J (2011) High gold concentrations in sulphide-bearing magma under oxidizing conditions. Nat Geosci 4:112–115

Burnham CW (1979) Magmas and hydrothermal fluids. Geochemistry of Hydrothermal Ore Deposits, 2nd ed, p. 71–136

Candela PA (1992) Controls on ore metal ratios in granite-related ore systems: an experimental and computational approach. Earth Environ Sci Trans R Soc Edinb 83:317–326

Cao K, Yang Z-M, Xu J-F, Fu B, Li W-K, Sun M-Y (2018) Origin of dioritic magma and its contribution to porphyry Cu–Au mineralization at Pulang in the Yidun arc, eastern Tibet. Lithos 304–307:436–449. https://doi.org/10.1016/j.lithos.2018.02.018

Cao K, Yang Z-M, Mavrogenes J, White NC, Xu J-F, Li Y, Li W-K (2019) Geology and genesis of the giant Pulang porphyry Cu–Au district, Yunnan, Southwest China. Econ Geol 114:275–301. https://doi.org/10.5382/econgeo.2019.4631

Cawood PA, Zhao GC, Yao JL, Wang W, Xu YJ, Wang YJ (2018) Reconstructing South China in Phanerozoic and Precambrian supercontinents. Earth-Sci Rev 186:173–194. https://doi.org/10.1016/j.earscirev.2017.06.001

Chang C (1997) Geology and Tectonics of Qinghai-Xizang Plateau–Solid Earth Sciences Research in China. Science Press, Beijing, pp 1–153 (in Chinese with English abstract)

Chang EZ (2000) Geology and tectonics of the Songpan–Ganzi fold belt, southwestern China. Int Geol Rev 42:813–831. https://doi.org/10.1080/00206810009465113

Chen JL, Xu JF, Ren JB, Huang XX, Wang BD (2014) Geochronology and geochemical characteristics of Late Triassic porphyritic rocks from the Zhongdian arc, eastern Tibet, and their tectonic and metallogenic implications. Gondwana Res 26:492–504. https://doi.org/10.1016/j.gr.2013.07.022

Chen JL, Xu JF, Ren JB, Huang XX (2017) Late Triassic E-MORB-like basalts associated with porphyry Cu-deposits in the southern Yidun continental arc, eastern Tibet: evidence of slab-tear during subduction? Ore Geol Rev 90:1054–1062. https://doi.org/10.1016/j.oregeorev.2016.12.006

Chiaradia M, Schaltegger U, Spikings R, Wotzlaw J-F, Ovtcharova M (2013) How accurately can we date the duration of magmatic-hydrothermal events in porphyry systems?—an invited paper. Econ Geol 108:565–584. https://doi.org/10.2113/econgeo.108.4.565

Chiaradia M (2014) Copper enrichment in arc magmas controlled by overriding plate thickness. Nature Geosci 7:43–46. https://doi.org/10.1038/ngeo2028

Dai L-Q, Zheng F, Zhao Z-F, Zheng Y-F (2017) Recycling of Paleo-tethyan oceanic crust: geochemical record from postcollisional mafic igneous rocks in the Tongbai-Hong'an orogens. Geol Soc Am Bull 129:179–192. https://doi.org/10.1130/B31461.1

Deng J, Hou ZQ, Mo XX, Yang LQ, Wang QF, Wang CM (2010) Superimposed orogenesis and metallogenesis in Sanjiang Tethys. Mineral Deposits 29:37–42 (in Chinese with English abstract)

Deng J, Wang Q, Li G, Li C, Wang C (2014) Tethys tectonic evolution and its bearing on the distribution of important mineral deposits in the Sanjiang region, SW China. Gondwana Res 26:419–437. https://doi.org/10.1016/j.gr.2013.08.002

Deng J, Wang CM, Zi JW, Xia R, Li Q (2018) Constraining subduction-collision processes of the Paleo-Tethys along the Changning-Menglian Suture: new zircon U-Pb ages and Sr-Nd-Pb-Hf-O isotopes of the Lincang batholith. Gondwana Res 62:75–92. https://doi.org/10.1016/j.gr.2017.10.008

Deng XD, Li JW, Luo T, Wang HQ (2017) Dating magmatic and hydrothermal processes using andradite-rich garnet U-Pb geochronometry. Contrib Mineral Petrol 172:71. https://doi.org/10.1007/s00410-017-1389-2

Dilles JH, Kent AJR, Wooden JL, Tosdal RM, Koleszar A, Lee RG, Farmer LP (2015) Zircon compositional evidence for sulfur-degassing from ore-forming arc magmas. Econ Geol 110:241–251. https://doi.org/10.2113/econgeo.110.1.241

Dong G, Mo X, Zhao Z, Zhu D, Goodman RC, Kong H, Wang S (2013) Zircon U-Pb dating and the petrological and geochemical constraints on Lincang granite in western Yunnan, China: implications for the closure of the Paleo-Tethys Ocean. J Asian Earth Sci 62:282–294. https://doi.org/10.1016/j.jseaes.2012.10.003

Fan WM, Wang YJ, Zhang AM, Zhang FF, Zhang YZ (2010) Permian arc-back-arc basin development along the Ailaoshan tectonic zone: geochemical, isotopic and geochronological evidence from the Mojiang volcanic rocks, southwest China. Lithos 119:553–568. https://doi.org/10.1016/j.lithos.2010.08.010

Fang W, Dai L-Q, Zheng Y-F, Zhao Z-F, Chen Q, Zhou Y (2020) Syn-exhumation magmatism in an active continental margin above a continental subduction zone: evidence from Late Triassic mafic igneous rocks in the southeastern North China Block. Geol Soc Am Bull. https://doi.org/10.1130/B35656.1

Ferry JM, Watson EB (2007) New thermodynamic models and revised calibrations for the Ti-in-zircon and Zr-in-rutile thermometers. Contrib Mineral Petrol 154:429–437. https://doi.org/10.1007/s00410-007-0201-0

Gao R, Xiao L, He Q, Yuan J, Ni PZ, Du JX (2010) Geochronology, geochemistry and petrogenesis of granites in Weixi–Deqin, west Yunnan. Earth Sci–J China U Geosci 35:186–200 (in Chinese with English abstract)

Green TH, Pearson NJ (1985) Experimental determination of REE partition coefficients between amphibole and basaltic to andesitic liquids at high pressure. Geochim Cosmochim Acta 49:1465–1468

Griffin W, Wang X, Jackson S, Pearson N, O'Reilly SY, Xu X, Zhou X (2002) Zircon chemistry and magma mixing, SE China: in-situ analysis of Hf isotopes, Tonglu and Pingtan igneous complexes. Lithos 61:237–269

Gustafson LB, Hunt JP (1975) The porphyry copper deposit at El Salvador, Chile. Econ Geol 70:857–912

Hamlyn PR, Keays RR, Cameron WE, Crawford AJ, Waldron HM (1985) Precious metals in magnesian low-Ti lavas: implications for metallogenesis and sulfur saturation in primary magmas. Geochim Cosmochim Acta 49:1797–1811

Hawkesworth CJ, Gallagher K, Hergt JM, Mcdermott F (1993) Mantle and slab contributions in ARC magmas. Annu Rev Earth Planet Sci 21:175–204

Hawkesworth CJ, Turner SP, McDermott F, Peate DW, vanCalsteren P (1997) U-Th isotopes in arc magmas: implications for element transfer from the subducted crust. Science 276:551–555. https://doi.org/10.1126/science.276.5312.551

He W, Yang L, Lu Y, Jeon H, Xie S, Gao X (2018) Zircon U–Pb dating, geochemistry and Sr–Nd–Hf–O isotopes for the Baimaxueshan granodiorites and mafic microgranulars enclaves in the Sanjiang Orogen: evidence for westward subduction of Paleo-Tethys. Gondwana Res 62:112–126. https://doi.org/10.1016/j.gr.2018.03.011

Hennig D, Lehmann B, Frei D, Belyatsky B, Zhao XF, Cabral AR, Zeng PS, Zhou MF, Schmidt K (2009) Early Permian seafloor to continental arc magmatism in the eastern Paleo-Tethys: U-Pb age and Nd-Sr isotope data from the southern Lancangjiang zone, Yunnan, China. Lithos 113:408–422. https://doi.org/10.1016/j.lithos.2009.04.031

Hildreth W, Moorbath S (1988) Crustal contributions to arc magmatism in the Andes of Central Chile. Contrib Mineral Petrol 98:455–489. https://doi.org/10.1007/BF00372365

Hoskin PWO, Schaltegger U (2003) The composition of zircon and igneous and metamorphic petrogenesis. In: Hanchar JM, Hoskin PWO (eds) Zircon, Rev Mineral Geochem, vol 53, pp 27–62

Hou ZQ, Mo XX, Tan J, Hu SH, Luo ZW (1993) The eruption sequences of basalts in the Yidun island-arc, Sanjiang region and evolution of rift to island-arc. Bull Chinese Acad Geol Sci 26:49–67 (in Chinese)

Hou ZQ, Yang YQ, Wang HP, Qu XM, Lü QT, Huang DH, Wu XZ, Tang SH, Zhao JH (2003) Collision-orogenic progress and mineralization system of Yidun Arc. Geological Publishing House, Beijing (in Chinese)

Hou Z, Yang Z, Lu Y, Kemp A, Zheng Y, Li Q, Tang J, Yang Z, Duan L (2015) A genetic linkage between subduction- and collision-related porphyry Cu deposits in continental collision zones. Geology 43:643–650

Hou Z, Zhou Y, Wang R, Zheng Y, He W, Zhao M, Evans NJ, Weinberg RF (2017) Recycling of metal-fertilized lower continental crust: origin of non-arc Au-rich porphyry deposits at cratonic edges. Geology 45:563–566

Huang B, Yan Y, Piper JDA, Zhang D, Yi Z, Yu S, Zhou T (2018) Paleomagnetic constraints on the paleogeography of the East

Asian blocks during Late Paleozoic and Early Mesozoic times. Earth-Sci Rev 186:8–36

Huang XL, Xu YG, Lan JB, Yang QJ, Luo ZY (2009) Neoproterozoic adakitic rocks from Mopanshan in the western Yangtze Craton: partial melts of a thickened lower crust. Lithos 112:367–381. https://doi.org/10.1016/j.lithos.2009.03.028

Jian P, Liu D, Kröner A, Zhang Q, Wang Y, Sun X, Zhang W (2009a) Devonian to Permian plate tectonic cycle of the Paleo-Tethys Orogen in southwest China (II): insights from zircon ages of ophiolites, arc/back-arc assemblages and within-plate igneous rocks and generation of the Emeishan CFB province. Lithos 113:767–784. https://doi.org/10.1016/j.lithos.2009.04.006

Jian P, Liu D, Kröner A, Zhang Q, Wang Y, Sun X, Zhang W (2009b) Devonian to Permian plate tectonic cycle of the Paleo-Tethys Orogen in southwest China (I): geochemistry of ophiolites, arc/back-arc assemblages and within-plate igneous rocks. Lithos 113: 748–766. https://doi.org/10.1016/j.lithos.2009.04.004

Jian X, Weislogel A, Pullen A (2019) Triassic sedimentary filling and closure of the eastern Paleo-Tethys Ocean: new insights from detrital zircon geochronology of Songpan–Ganzi, Yidun, and West Qinling flysch in eastern Tibet. Tectonics 38:767–787. https://doi.org/10.1029/2018tc005300

Jin CH, Fan WY, Zhang Y, Zhang H, Shen ZW, Gao JH (2013) Trace element composition and U-Pb chronology of zircons in monzonite porphyry from the Langdu copper deposit in Zhongdian and their geological significance. Geotectonica et Metallogenia 37:262–272 (in Chinese with English abstract)

Jugo PJ (2009) Sulfur content at sulfide saturation in oxidized magmas. Geology 37:415–418

Kay SM, Mpodozis C (2001) Central Andean ore deposits linked to evolving shallow subduction systems and thickening crust. GSA Today 11:4

Keto LS, Jacobsen SB (1987) Nd and Sr isotopic variations of Early Paleozoic oceans. Earth Planet Sci Lett 84:27–41

Kong D-X, Xu J-F, Chen J-L (2016) Oxygen isotope and trace element geochemistry of zircons from porphyry copper system: implications for Late Triassic metallogenesis within the Yidun Terrane, southeastern Tibetan Plateau. Chem Geol 441:148–161. https://doi.org/10.1016/j.chemgeo.2016.08.012

KPDI <Kunming Prospecting Design Institute of China Nonferrous Metals Industry> (2014) Exploration report of Pulang copper deposit. Yunnan Diqing Nonferrous Metal Co. Ltd., Yunnan

Lai AQ, Li WC, Liu XL, Yang FC, Li Z (2016) Zircon U-Pb dating, geochemical characteristics of Songnuo quartz monzonite porphyries in the Geza Arc, Yunnan Province, and their geological significance. Geol Rev 62:955–969 (in Chinese with English abstract)

Lee R, Dilles J, Tosdal RL, Wooden J, Mazdab KF (2017) Magmatic evolution of granodiorite intrusions at the El Salvador porphyry copper deposit, Chile, based on trace element composition and U/Pb age of zircons. Econ Geol 112:245–273

Leng CB, Zhang XC, Hu RZ, Wang SX, Zhong H, Wang WQ, Bi XW (2012) Zircon U-Pb and molybdenite Re-Os geochronology and Sr–Nd–Pb–Hf isotopic constraints on the genesis of the Xuejiping porphyry copper deposit in Zhongdian, Northwest Yunnan, China. J Asian Earth Sci 60:31–48. https://doi.org/10.1016/j.jseaes.2012.07.019

Leng CB, Huang QY, Zhang XC, Wang SX, Zhong H, Hu RZ, Bi XW, Zhu JJ, Wang X-S (2014) Petrogenesis of the Late Triassic volcanic rocks in the Southern Yidun arc, SW China: constraints from the geochronology, geochemistry, and Sr–Nd–Pb–Hf isotopes. Lithos 190–191:363–382. https://doi.org/10.1016/j.lithos.2013.12.018

Leng CB, Gao JF, Chen WT, Zhang XC, Tian ZD, Guo JH (2018) Platinum-group elements, zircon Hf-O isotopes, and mineralogical constraints on magmatic evolution of the Pulang porphyry Cu-Au system, SW China. Gondwana Res 62:163–177. https://doi.org/10.1016/j.gr.2018.03.001

Li C, Ripley EM, Tao Y, Hu R (2016) The significance of PGE variations with Sr–Nd isotopes and lithophile elements in the Emeishan flood basalt province from SW China to northern Vietnam. Lithos 248–251:1–11. https://doi.org/10.1016/j.lithos.2015.12.027

Li GJ, Wang QF, Yu L, Hu ZC, Ma N, Huang YH (2013a) Closure time of the Ailaoshan Paleo-Tethys Ocean: constraints from the zircon U-Pb dating and geochemistry of the Late Permian granitoids. Acta Petrol Sin 29:3883–3900 (in Chinese with English abstract)

Li S, Chung S-L, Hou Z, Chew D, Wang T, Wang B, Wang Y (2019a) Early Mesozoic magmatism within the Tibetan Plateau: implications for the Paleo-Tethyan tectonic evolution and continental amalgamation. Tectonics 38:3505–3543. https://doi.org/10.1029/2019TC005546

Li WC, Zeng PS, Hou ZQ, Noel CW (2011) The Pulang porphyry copper deposit and associated felsic intrusions in Yunnan Province, Southwest China. Econ Geol 106:79–92

Li W, Yang Z, Cao K, Lu Y, Sun M (2019b) Redox-controlled generation of the giant porphyry Cu–Au deposit at Pulang, southwest China. Contrib Mineral Petrol 174:12. https://doi.org/10.1007/s00410-019-1546-x

Li XH, Long WG, Li QL, Liu Y, Tao H (2010) Penglai zircon megacrysts: a potential new working reference material for microbeam determination of Hf–O isotopes and U–Pb age. Geostand Geoanalyt Res 34:117–134

Li XH, Tang GQ, Gong B, Yang YH, Hou KJ, Hu ZC, Li QL, Liu Y, Li WX (2013b) Qinghu zircon: a working reference for microbeam analysis of U-Pb age and Hf and O isotopes. Chin Sci Bull 58: 4647–4654. https://doi.org/10.1007/s11434-013-5932-x

Liang HY, Campbell IH, Allen C, Sun WD, Liu CQ, Yu HX, Xie YW, Zhang YQ (2006) Zircon Ce^{4+}/Ce^{3+} ratios and ages for Yulong ore-bearing porphyries in eastern Tibet. Miner Deposita 41:152–159. https://doi.org/10.1007/s00126-005-0047-1

Liang Q, Jing H, Gregoire DC (2000) Determination of trace elements in granites by inductively coupled plasma mass spectrometry. Talanta 51:507–513. https://doi.org/10.1016/S0039-9140(99)00318-5

Liu C, Deng JF, Liu JL, Shi YL (2011) Characteristics of volcanic rocks from Late Permian to Early Traissic in Ailaoshan tectono-magmatic belt and implications for tectonic settings. Acta Petrol Sin 27:3590–3602

Liu CJ, Diao ZZ, Zhang ZG (1994) Tethyan Geology of Western Sichuan and Eastern Tibet. Southwest Jiaotong University Press, Chengdu (in Chinese with English abstract)

Liu HC, Wang YJ, Cawood PA, Fan W, Cai Y, Xing X (2015) Record of Tethyan ocean closure and Indosinian collision along the Ailaoshan suture zone (SW China). Gondwana Res 27:1292–1306. https://doi.org/10.1016/j.gr.2013.12.013

Liu HC, Wang YJ, Li ZH, Zi JW, Huangfu PP (2018) Geodynamics of the Indosinian orogeny between the South China and Indochina blocks: insights from latest Permian–Triassic granitoids and numerical modeling. Geol Soc Am Bull 130:1289–1306. https://doi.org/10.1130/b31904.1

Liu HC, Liu XP, Zhang YW, Yu ZQ, Wang K (2020) Beginning of the Indosinian Orogeny: insights from Late Permian gabbro and diorite in the Diancangshan area of the Yunnan province. Geotectonica et Metallogenia 44:527–542 (in Chinese with English abstract)

Liu YS, Gao S, Hu ZC, Gao CG, Zong KQ, Wang DB (2010a) Continental and oceanic crust recycling-induced melt-peridotite interactions in the trans-north China Orogen: U-Pb dating, Hf Isotopes and trace elements in zircons from mantle xenoliths. J Petrol 51: 537–571. https://doi.org/10.1093/petrology/egp082

Liu YS, Hu ZC, Zong KQ, Gao CG, Gao S, Xu JA, Chen HH (2010b) Reappraisement and refinement of zircon U-Pb isotope and trace element analyses by LA-ICP-MS. Chin Sci Bull 55:1535–1546. https://doi.org/10.1007/s11434-010-3052-4

Loader MA, Wilkinson JJ, Armstrong RN (2017) The effect of titanite crystallisation on Eu and Ce anomalies in zircon and its implications

for the assessment of porphyry Cu deposit fertility. Earth Planet Sci Lett 472:107–119. https://doi.org/10.1016/j.epsl.2017.05.010

Loucks R (2014) Distinctive composition of copper-ore-forming arcmagmas. Aust J Earth Sci 61:5–16

Loucks RR, Fiorentini ML, Rohrlach BD (2018) Divergent T–$fO2$ paths during crystallisation of H_2O-rich and H_2O-poor magmas as recorded by Ce and U in zircon, with implications for TitaniQ and TitaniZ geothermometry. Contrib Mineral Petrol 173:104

Loucks RR, Fiorentini ML, Henriquez GJ (2020) New magmatic oxybarometer using trace elements in zircon. J Petrol 61(3):1–30. https://doi.org/10.1093/petrology/egaa034

Lu YJ, Loucks RR, Fiorentini M, McCuaig TC, Evans NJ, Yang Z-M, Hou Z-Q, Kirkland CL, Parra-Avila LA, Kobussen A (2016) Zircon compositions as a pathfinder for porphyry Cu ± Mo ± Au deposits. In: Richards JP (ed) Tectonics and Metallogeny of the Tethyan Orogenic Belt. Society of Economic Geologists 19:329–347

Meng E, Liu FL, Du LL, Liu PH, Liu JH (2015) Petrogenesis and tectonic significance of the Baoxing granitic and mafic intrusions, southwestern China: evidence from zircon U-Pb dating and Lu-Hf isotopes, and whole-rock geochemistry. Gondwana Res 28:800–815. https://doi.org/10.1016/j.gr.2014.07.003

Meng X, Mao J, Zhang C, Zhang D, Liu H (2018) Melt recharge, fO_2 -T conditions, and metal fertility of felsic magmas: zircon trace element chemistry of Cu-Au porphyries in the Sanjiang orogenic belt, southwest China. Miner Deposita 53:1–15

Metcalfe I (2002) Permian tectonic framework and palaeogeography of SE Asia. J Asian Earth Sci 20:551–566. https://doi.org/10.1016/s1367-9120(02)00022-6

Metcalfe I (2013) Gondwana dispersion and Asian accretion: tectonic and palaeogeographic evolution of eastern Tethys. J Asian Earth Sci 66:1–33

Mo XX, Lu FX, Shen SY (1993) Sanjiang Tethyan volcanism and related mineralization. Geological Press, Beijing, pp 1–267 (in Chinese)

Mo XX, Sheng S, Zhu Q (1998) Volcanics, Ophiolite and Mineralization of Middle-Southern Part in Sanjiang Area of Southwest China. Geological Press, Beijing (in Chinese with English abstract)

Moore G, Carmichael ISE (1998) The hydrous phase equilibria (to 3 kbar) of an andesite and basaltic andesite from western Mexico: constraints on water content and conditions of phenocryst growth. Contrib Mineral Petrol 130:304–319

Naney MT (1983) Phase equilibria of rock-forming ferromagnesian silicates in granitic systems. Am J Sci 283:993–1033

Pan G, Wang L, Li R, Yuan S, Ji W, Yin F, Zhang W, Wang B (2012) Tectonic evolution of the Qinghai-Tibet Plateau. J Asian Earth Sci 53:3–14

Pang ZS, Du YS, Wang GW, Guo Y, Li Q (2009) Single-grain zircon U-Pb isotopic ages, geochemistry and its implication of the Pulang complex in Yunnan Province, China. Acta Petrol Sin 25:159–165

Patchett PJ, Tatsumoto M (1981) A routine high-precision method for Lu-Hf isotope geochemistry and chronology. Contrib Mineral Petrol 75:263–267. https://doi.org/10.1007/BF01166766

Pearce JA (1996) Sources and settings of granitic rocks. Episodes 19:120–125

Pearce NJG, Perkins WT, Westgate JA, Gorton MP, Jackson SE, Neal CR, Chenery SP (1997) A compilation of new and published major and trace element data for NIST SRM 610 and NIST SRM 612 glass reference materials. Geostand Newsl 21:115–144. https://doi.org/10.1111/j.1751-908X.1997.tb00538.x

Peng T, Wilde SA, Wang Y, Fan W, Peng B (2013) Mid-Triassic felsic igneous rocks from the southern Lancangjiang Zone, SW China: petrogenesis and implications for the evolution of Paleo-Tethys. Lithos 168–169:15–32. https://doi.org/10.1016/j.lithos.2013.01.015

Peng T, Zhao G, Fan W, Peng B, Mao Y (2014) Zircon geochronology and Hf isotopes of Mesozoic intrusive rocks from the Yidun terrane, eastern Tibetan Plateau: petrogenesis and their bearings with Cu mineralization. J Asian Earth Sci 80:18–33

Peng T, Zhao G, Fan W, Peng B, Mao Y (2015) Late Triassic granitic magmatism in the eastern Qiangtang, eastern Tibetan Plateau: geochronology, petrogenesis and implications for the tectonic evolution of the Paleo-Tethys. Gondwana Res 27:1494–1508. https://doi.org/10.1016/j.gr.2014.01.009

Pilet S, Baker MB, Muntener O, Stolper EM (2011) Monte carlo simulations of metasomatic enrichment in the lithosphere and implications for the source of alkaline basalts. J Petrol 52:1415–1442. https://doi.org/10.1093/petrology/egr007

Reid AJ, Wilson CJL, Liu S (2005) Structural evidence for the Permo-Triassic tectonic evolution of the Yidun arc, eastern Tibetan plateau. J Struct Geol 27:119–137. https://doi.org/10.1016/j.jsg.2004.06.011

Reid AJ, Wilson CJL, Shun L, Pearson N, Belousova E (2007) Mesozoic plutons of the Yidun arc, SW China: U/Pb geochronology and Hf isotopic signature. Ore Geol Rev 31:88–106. https://doi.org/10.1016/j.oregeorev.2004.11.003

Rezeau H, Moritz R, Wotzlaw JF, Hovakimyan S, Tayan R (2019) Zircon petrochronology of the Meghri-Ordubad Pluton, Lesser Caucasus: fingerprinting igneous processes and implications for the exploration of porphyry Cu-Mo deposits. Econ Geol 114:1365–1388

Richards JP (2003) Tectono-magmatic precursors for porphyry Cu-(Mo-Au) deposit formation. Econ Geol 98:1515–1533. https://doi.org/10.2113/98.8.1515

Richards JP, Kerrich R (2007) Special paper: adakite-like rocks: their diverse origins and questionable role in metallogenesis. Econ Geol 102:537–576. https://doi.org/10.2113/gsecongeo.102.4.537

Richards JP (2009) Postsubduction porphyry Cu-Au and epithermal Au deposits: products of remelting of subduction-modified lithosphere. Geology 37:247–250. https://doi.org/10.1130/g25451a.1

Richards JP (2011a) High Sr/Y arc magmas and porphyry Cu +/- Mo +/- Au deposits: just add water. Econ Geol 106:1075–1081. https://doi.org/10.2113/econgeo.106.7.1075

Richards JP (2011b) Magmatic to hydrothermal metal fluxes in convergent and collided margins. Ore Geol Rev 40:1–26. https://doi.org/10.1016/j.oregeorev.2011.05.006

Richards JP, Spell T, Rameh E, Razique A, Fletcher T (2012) High Sr/Y magmas reflect arc maturity, high magmatic water content, and porphyry Cu ± Mo ± Au potential: examples from the tethyan arcs of central and eastern Iran and western Pakistan. Econ Geol 107:295–332

Richards JP (2015) The oxidation state, and sulfur and Cu contents of arc magmas: implications for metallogeny. Lithos 233:27–45. https://doi.org/10.1016/j.lithos.2014.12.011

Richards JP, Şengör AMC (2017) Did Paleo-Tethyan anoxia kill arc magma fertility for porphyry copper formation? Geology 45:591–594

Ridolfi F, Renzulli A, Puerini M (2010) Stability and chemical equilibrium of amphibole in calc-alkaline magmas: an overview, new thermobarometric formulations and application to subduction-related volcanoes. Contrib Mineral Petrol 160:45–66

Roger F, Jolivet M, Malavieille J (2010) The tectonic evolution of the Songpan-Garzê (North Tibet) and adjacent areas from Proterozoic to present: a synthesis. J Asian Earth Sci 39:254–269. https://doi.org/10.1016/j.jseaes.2010.03.008

Scherer E, Münker C, Mezger K (2001) Calibration of the lutetiumhafnium clock. Science 293:683–687

Seedorff E, Dilles J, Proffett JM, Einaudi MT, Zurcher L, Stavast WJA, Johnson DA, Barton M (2005) Porphyry deposits: characteristics and origin of hypogene features. Porphyry deposits: characteristics and origin of hypogene features 100th Anniversary Volume:251–298

Seman S, Stockli DF, McLean NM (2017) U-Pb geochronology of grossular-andradite garnet. Chem Geol 460:106–116. https://doi.org/10.1016/j.chemgeo.2017.04.020

Şengör AMC (1979) Mid-Mesozoic closure of Permo–Triassic Tethys and its implications. Nature 279:590–593. https://doi.org/10.1038/279590a0

Şengör AMC, Cin A, Rowley DB, Nie SY (1993) Space-time patterns of magmatism along the Tethysides—a preliminary-study. J Geol 101:51–84. https://doi.org/10.1086/648196

Sillitoe RH (2010) Porphyry copper systems. Econ Geol 105:3–41

Slama J, Kosler J, Condon DJ, Crowley JL, Gerdes A, Hanchar JM, Horstwood MSA, Morris GA, Nasdala L, Norberg N, Schaltegger U, Schoene B, Tubrett MN, Whitehouse MJ (2008) Plesovice zircon—a new natural reference material for U-Pb and Hf isotopic microanalysis. Chem Geol 249:1–35. https://doi.org/10.1016/j.chemgeo.2007.11.005

Smythe DJ, Brenan JM (2015) Cerium oxidation state in silicate melts: combined fO_2, temperature and compositional effects. Geochim Cosmochim Acta 170:173–187. https://doi.org/10.1016/j.gca.2015.07.016

Smythe DJ, Brenan JM (2016) Magmatic oxygen fugacity estimated using zircon-melt partitioning of cerium. Earth Planet Sci Lett 453:260–266. https://doi.org/10.1016/j.epsl.2016.08.013

Song XY, Zhou M-F, Cao ZM, Robinson P (2004) Late Permian rifting of the south China craton caused by the Emeishan mantle plume? J Geol Soc 161:773–781. https://doi.org/10.1144/0016-764903-135

Sun M, Yin A, Yan D, Ren H, Mu H, Zhu L, Qiu L (2018) Role of pre-existing structures in controlling the Cenozoic tectonic evolution of the eastern Tibetan plateau: new insights from analogue experiments. Earth Planet Sci Lett 491:207–215. https://doi.org/10.1016/j.epsl.2018.03.005

Sun SS, McDonough WS (1989) Chemical and isotopic systematics of oceanic basalts: implications for mantle composition and processes. Geo Soc London Special Pub 42:313–345

Sun W, Wang J-t, L-p Z, C-c Z, Li H, M-x L, Ding X, C-y L, Liang H-y (2017) The formation of porphyry copper deposits. Acta Geochimica 36:9–15. https://doi.org/10.1007/s11631-016-0132-4

Tian ZD, Leng CB, Zhang XC (2020) Provenance and tectonic setting of the Neoproterozoic meta-sedimentary rocks at southeastern Tibetan Plateau: implications for the tectonic affinity of Yidun terrane. Precambrian Res 344:105736. https://doi.org/10.1016/j.precamres.2020.105736

Trail D, Bruce Watson E, Tailby ND (2012) Ce and Eu anomalies in zircon as proxies for the oxidation state of magmas. Geochim Cosmochim Acta 97:70–87. https://doi.org/10.1016/j.gca.2012.08.032

Vervoort JD, Patchett PJ, Soderlund U, Baker M (2004) Isotopic composition of Yb and the determination of Lu concentrations and Lu/Hf ratios by isotope dilution using MC-ICPMS. Geochemistry Geophys Geosystems 5:15. https://doi.org/10.1029/2004gc000721

Wang BD, Wang LQ, Chen JL, Yin FG, Wang DB, Zhang WP, Chen LK, Liu H (2014a) Triassic three-stage collision in the Paleo-Tethys: constraints from magmatism in the Jiangda-Deqen-Weixi continental margin arc, SW China. Gondwana Res 26:475–491. https://doi.org/10.1016/j.gr.2013.07.023

Wang BQ, Zhou MF, Li JW, Yan DP (2011) Late Triassic porphyritic intrusions and associated volcanic rocks from the Shangri-La region, Yidun terrane, eastern Tibetan Plateau: adakitic magmatism and porphyry copper mineralization. Lithos 127:24–38. https://doi.org/10.1016/j.lithos.2011.07.028

Wang BQ, Wang W, Chen WT, Gao JF, Zhao XF, Yan DP, Zhou MF (2013) Constraints of detrital zircon U-Pb ages and Hf isotopes on the provenance of the Triassic Yidun group and tectonic evolution of the Yidun terrane, eastern Tibet. Sediment Geol 289:74–98. https://doi.org/10.1016/j.sedgeo.2013.02.005

Wang JH, Li WC (2014) The geochemical correlation between Songnuo and Pulang porphyry body in Xianggelila. Geology of Yunnan 33:185–187 (in chinese)

Wang P, Dong GC, Zhao GC, Han YG, Li YP (2018a) Petrogenesis of the Pulang porphyry complex, southwestern China: implications for porphyry copper metallogenesis and subduction of the Paleo-Tethys Oceanic lithosphere. Lithos 304–307:280–297. https://doi.org/10.1016/j.lithos.2018.02.009

Wang Q, Xu JF, Jian P, Bao ZW, Zhao ZH, Li CF, Xiong XL, Ma JL (2006) Petrogenesis of adakitic porphyries in an extensional tectonic setting, dexing, South China: implications for the genesis of porphyry copper mineralization. J Petrol 47:119–144. https://doi.org/10.1093/petrology/egi070

Wang Q, Wyman DA, Xu J, Wan Y, Li C, Zi F, Jiang Z, Qiu H, Chu Z, Zhao Z, Dong Y (2008) Triassic Nb-enriched basalts, magnesian andesites, and adakites of the Qiangtang terrane (Central Tibet): evidence for metasomatism by slab-derived melts in the mantle wedge. Contrib Mineral Petrol 155:473–490. https://doi.org/10.1007/s00410-007-0253-1

Wang R, Richards JP, Z-q H, Yang Z-m, Gou Z-h, DuFrane SA (2014b) Increasing magmatic oxidation state from paleocene to miocene in the eastern Gangdese Belt, Tibet: implication for collision-related porphyry Cu-Mo±Au mineralization. Econ Geol 109:1943–1965

Wang R, Richards JP, Hou ZQ, Yang ZM, DuFrane SA (2014c) Increased magmatic water content-the Key to Oligo-Miocene porphyry Cu-Mo +/- Au formation in the eastern Gangdese belt, Tibet. Econ Geol 109:1315–1339. https://doi.org/10.2113/econgeo.109.5.1315

Wang X, Wang S, Wang C, Tang W (2018b) Permo-Triassic arc-like granitoids along the northern Lancangjiang zone, eastern Tibet: age, geochemistry, Sr–Nd–Hf isotopes, and tectonic implications. Lithos 308–309:278–293. https://doi.org/10.1016/j.lithos.2018.03.008

Wang Y, Qian X, Cawood PA, Liu H, Feng Q, Zhao G, Zhang Y, He H, Zhang P (2018c) Closure of the east Paleotethyan Ocean and amalgamation of the eastern Cimmerian and southeast Asia continental fragments. Earth-Sci Rev 186:195–230. https://doi.org/10.1016/j.earscirev.2017.09.013

Wang Y, Wang Q, Deng J, Xue S, Li C, Ripley EM (2020a) Triassic arc mafic magmatism in north Qiangtang: implications for tectonic reconstruction and mineral exploration. Gondwana Res 82:337–352. https://doi.org/10.1016/j.gr.2020.01.013

Wang Y, Zhang H, Zhang H, Chai P, Hou Z (2020b) Gold in the lithosphere of the western south China block, SW China: insights from quartz porphyries from the giant Zhenyuan gold deposit. Ore Geol Rev 119:103312. https://doi.org/10.1016/j.oregeorev.2020.103312

Wasserburg G, Jacobsen S, McCulloch M, Wen T (1981) Precise determination of Sm/Nd ratios, Sm and Nd isotopic abundances in standard solutions. Geochim Cosmochim Acta 45:2311–2323. https://doi.org/10.1016/0016-7037(81)90085-5

Weis D, Kieffer B, Maerschalk C, Barling J, De Jong J, Williams G, Hanano D, Pretorius W, Mattielli N, Scoates J, Goolaerts A, Friedman R, Mahoney J (2006) High-precision isotopic characterization of USGS reference materials by TIMS and MC-ICP-MS. Geochemistry Geophys Geosystems 7:1–30. https://doi.org/10.1029/2006GC001283

White WM, Hofmann AW (1982) Sr and Nd isotope geochemistry of oceanic basalts and mantle evolution. Nature 296:821–825

Wiedenbeck M, Alle P, Corfu F, Griffin WL, Meier M, Oberli F, Vonquadt A, Roddick JC, Speigel W (1995) Three natural zircon standards for U–Th–Pb, Lu–Hf, trace element and REE analysis. Geostand Newsl 19:1–23. https://doi.org/10.1111/j.1751-908X.1995.tb00147.x

Wilkinson JJ (2013) Triggers for the formation of porphyry ore deposits in magmatic arcs. Nat Geosci 6:917–925. https://doi.org/10.1038/ngeo1940

Winchester JA, Floyd PA (1977) Geochemical discrimination of different magma series and their differentiation products using immobile

elements. Chem Geol 20:325–343. https://doi.org/10.1016/0009-2541(77)90057-2

Wu J, Dong T (2013) The metallogenesis feature of songnuo Cu multi-metallic orefield in zhongdian,Yunnan. Geology of Yunnan 32: 409–411 (in Chinese)

Wu T, Xiao L, Ma CQ, Huang W (2013) The geochronological, geochemical and Sr-Nd isotopic characteristics of Tongpu intrusive complex and its implications. Acta petrol Sin 29:3567–3580 (in Chinese with English abstract)

Wu T, Xiao L, Wilde SA, Ma C-Q, Li Z-L, Sun Y, Zhan Q-Y (2016) Zircon U–Pb age and Sr–Nd–Hf isotope geochemistry of the Ganluogou dioritic complex in the northern Triassic Yidun arc belt, eastern Tibetan Plateau: implications for the closure of the Garzê-Litang Ocean. Lithos 248–251:94–108. https://doi.org/10.1016/j.lithos.2015.12.029

Wu YB, Zheng YF (2013) Tectonic evolution of a composite collision orogen: an overview on the Qinling–Tongbai–Hong'an–Dabie–Sulu orogenic belt in central China. Gondwana Res 23:1402–1428

Xiao L, Xu YG, Xu JF, He B, Pirajno FC (2005) Chemostratigraphy of flood basalts in the Garze-Litang region and Zhongza block: implications for western extension of the Emeishan Large Igneous Province, SW China. Acta Geol Sin 78:61–67

Xin D, Yang TN, Liang MJ, Xue CD, Han X, Liao C, Tang J (2018) Syn-subduction crustal shortening produced a magmatic flare-up in middle Sanjiang orogenic belt, southeastern Tibet Plateau: evidence from geochronology, geochemistry, and structural geology. Gondwana Res 62:93–111. https://doi.org/10.1016/j.gr.2018.03.009

Xu W, Liu F, Dong Y (2020) Cambrian to Triassic geodynamic evolution of central Qiangtang, Tibet. Earth-Sci Rev 201:103083. https://doi.org/10.1016/j.earscirev.2020.103083

Xu Y, Luo Z, Huang X, He B, Xiao L, Xie L, Shi Y (2008) Zircon U–Pb and Hf isotope constraints on crustal melting associated with the Emeishan mantle plume. Geochim Cosmochim Acta 72:3084–3104

Xu Z, Dilek Y, Cao H, Yang J, Robinson P, Ma C, Li H, Jolivet M, Roger F, Chen X (2015) Paleo-Tethyan evolution of Tibet as recorded in the east Cimmerides and west Cathaysides. J Asian Earth Sci 105: 320–337. https://doi.org/10.1016/j.jseaes.2015.01.021

Yan Y, Zhao Q, Zhang Y, Huang B, Zheng W, Zhang P (2019) Direct paleomagnetic constraint on the closure of Paleo-Tethys and its implications for linking the Tibetan and southeast Asian blocks. Geophys Res Lett 46:14368–14376. https://doi.org/10.1029/2019GL085473

Yang LQ, Gao X, Shu Q-H (2017) Multiple Mesozoic porphyry-skarn Cu (Mo–W) systems in Yidun Terrane, east Tethys: constraints from zircon U–Pb and molybdenite Re–Os geochronology. Ore Geol Rev 90:813–826. https://doi.org/10.1016/j.oregeorev.2017.01.030

Yang LQ, He W-Y, Gao X, Xie S-X, Yang Z (2018) Mesozoic multiple magmatism and porphyry–skarn Cu–polymetallic systems of the Yidun terrane, eastern Tethys: implications for subduction- and transtension-related metallogeny. Gondwana Res 62:144–162. https://doi.org/10.1016/j.gr.2018.02.009

Yang TN, Zhang HR, Liu YX, Wang ZL, Song YC, Yang ZS, Tian SH, Xie HQ, Hou KJ (2011) Permo-Triassic arc magmatism in central Tibet: evidence from zircon U–Pb geochronology, Hf isotopes, rare earth elements, and bulk geochemistry. Chem Geol 284:270–282. https://doi.org/10.1016/j.chemgeo.2011.03.006

Yang TN, Ding Y, Zhang HR, Fan JW, Liang MJ, Wang XH (2014) Two-phase subduction and subsequent collision defines the Paleotethyan tectonics of the southeastern Tibetan Plateau: evidence from zircon U-Pb dating, geochemistry, and structural geology of the Sanjiang orogenic belt, southwest China. Geol Soc Am Bull 126: 1654–1682. https://doi.org/10.1130/b30921.1

Yang ZM, Cooke D (2019) Porphyry copper deposits in China. Society of Economic Geologists 5:133–187

Yao JH, Zhu WG, Li C, Zhong H, Bai ZJ, Ripley EM, Li C (2018) Petrogenesis and ore genesis of the Lengshuiqing magmatic sulfide deposit in southwest China: constraints from chalcophile elements (PGE, Se) and Sr-Nd-Os-S Isotopes. Econ Geol 113:675–698. https://doi.org/10.5382/econgeo.2018.4566

Yin A, Harrison TM (2000) Geologic evolution of the Himalayan-Tibetan orogen. Annu Rev Earth Planet Sci 28:211–280. https://doi.org/10.1146/annurev.earth.28.1.211

Yu HJ (2018) Composite metallogenic system and exploration research of the Geza porphyry belt, SW China. PhD Dissertation, China University of Geosciences (in Chinese with English abstract)

Zeng PS, Mo XX, Yu XH, Hou ZQ, Xu QD, Wang HP, Li H, Yang CZ (2003) Porphyries and porphyry copper deposits in Zhongdian area, northwest Yunnan. Mineral Deposits 20:393–400 (in Chinese with English abstract)

Zhang HF, Zhang L, Harris N, Jin LL, Yuan HL (2006) U-Pb zircon ages, geochemical and isotopic compositions of granitoids in Songpan-Garze fold belt, eastern Tibetan Plateau: constraints on petrogenesis and tectonic evolution of the basement. Contrib Mineral Petrol 152: 75–88. https://doi.org/10.1007/s00410-006-0095-2

Zhang LY, Ding L, Pullen A, Xu Q, Liu DL, Cai FL, Yue YH, Lai QZ, Shi RD, Ducea MN, Kapp P, Chapman A (2014) Age and geochemistry of western Hoh-Xil-Songpan-Ganzi granitoids, northern Tibet: implications for the Mesozoic closure of the Paleo-Tethys ocean. Lithos 190:328–348. https://doi.org/10.1016/j.lithos.2013.12.019

Zhang ND, Cao YW, Liao YA, Zhao Y, Zhang HJ, Hu DJ, Zhang R, Wang LZ (1998) Geology and metallogeny in Garze–Litang Rift Zone. Geological Publishing House, Beijing (in Chinese)

Zhao GC, Wang YJ, Huang BC, Dong YP, Li SZ, Zhang GW, Yu S (2018a) Geological reconstructions of the East Asian blocks: from the breakup of Rodinia to the assembly of Pangea. Earth-Sci Rev 186:262–286. https://doi.org/10.1016/j.earscirev.2018.10.003

Zhao JH, Zhou MF (2007) Neoproterozoic adakitic plutons and arc magmatism along the western margin of the Yangtze block, south China. J Geol 115:675–689. https://doi.org/10.1086/521610

Zhao JH, Li QW, Liu H, Wang W (2018b) Neoproterozoic magmatism in the western and northern margins of the Yangtze Block (South China) controlled by slab subduction and subduction-transform-edge-propagator. Earth-Sci Rev 187:1–18. https://doi.org/10.1016/j.earscirev.2018.10.004

Zhao X, Yu XH, Mo XX, Zhang J, Lu BX (2004) Petrological and geochemical characteristics of Cenozoic alkali-rich porphyries and xenoliths hosted in western Yunnan province. Geoscience 18:217–228

Zhong D (1998) The Paleo-Tethyan Orogenic Belts, Western Yunnan and Sichuan Provinces. Science Press, Beijing (in Chinese)

Zhou MF, Yan DP, Kennedy AK, Li YQ, Ding J (2002) SHRIMP U-Pb zircon geochronological and geochemical evidence for Neoproterozoic arc-magmatism along the western margin of the Yangtze Block, South China. Earth Planet Sci Lett 196:51–67. https://doi.org/10.1016/s0012-821x(01)00595-7

Zhou Y, Hou ZQ, Zheng YC, Xu B, Wang R, Luo CH (2017) Granulite xenoliths in Liuhe area: evidence for composition and genetic mechanism of the lower crust from the Neoproterozoic to Cenozoic. Acta Petrol Sin 33:2143–2160

Zhu CY, Zhao GC, Sun M, Eizenhofer PR, Han YG, Liu Q, Liu DX (2017) Subduction between the Jiamusi and Songliao blocks: geochronological and geochemical constraints from granitoids within the Zhangguangcailing orogen, northeastern China. Lithosphere 9: 515–533. https://doi.org/10.1130/l618.1

Zhu JJ, Richards JP, Rees C, Creaser R, DuFrane SA, Locock A, Petrus JA, Lang J (2018) Elevated magmatic sulfur and chlorine contents in ore-forming magmas at the Red Chris porphyry Cu-Au deposit, northern British Columbia, Canada. Econ Geol 113:1047–1075. https://doi.org/10.5382/econgeo.2018.4581

Zi JW, Cawood PA, Fan WM, Tohver E, Wang YJ, McCuaig TC (2012a) Generation of Early Indosinian enriched mantle-derived granitoid pluton in the Sanjiang orogen (SW China) in response to closure of the Paleo-Tethys. Lithos 140:166–182. https://doi.org/10.1016/j.lithos.2012.02.006

Zi JW, Cawood PA, Fan WM, Wang YJ, Tohver E (2012b) Contrasting rift and subduction-related plagiogranites in the Jinshajiang ophiolitic melange, southwest China, and implications for the Paleo-Tethys. Tectonics 31:1–18. https://doi.org/10.1029/2011tc002937

Zi JW, Cawood PA, Fan WM, Tohver E, Wang YJ, Mccuaig TC, Peng TP (2013) Late Permian-Triassic magmatic evolution in the Jinshajiang orogenic belt, SW China and implications for orogenic processes following closure of the Paleo-Tethys. Am J Sci 313:81–112

Zou XY, Qin KZ, Han XL, Li GM, Evans NJ, Li ZZ, Yang W (2019) Insight into zircon REE oxy-barometers: a lattice strain model perspective. Earth Planet Sci Lett 506:87–96. https://doi.org/10.1016/j.epsl.2018.10.031